Seismological models based on a hybrid deep-learning strategy reveal tectonic features and earthquake risk in the Sichuan-Yunnan region

Ziyi Li[1,2], Lianqing Zhou[3*], Mengqiao Duan[3], Yanru An[4], Zheng Wu[4],

Lisheng Xu[1] & Shiyong Zhou[2]

1. Institute of Geophysics, China Earthquake Administration, Beijing 100081, China
2. School of Earth and Space Sciences, Peking University, Beijing 100871, China
3. Key Laboratory of Earthquake Prediction, Institute of Earthquake Forecasting, China Earthquake Administration, Beijing 100036, China
4. China Earthquake Networks Center, Beijing 100045, China

Corresponding author: Lianqing Zhou (zhoulq@ief.ac.cn)

Abstract

The Sichuan-Yunnan region is a critical tectonic zone for understanding continental deformation and seismic hazards. We developed a hybrid deep-learning strategy that integrates multi-scale phase picking and high-precision first-motion polarity identification, significantly improving regional seismic monitoring. This approach yielded a unified 2013-2022 high-resolution dataset, including -180,000 relocated events, 2,524 focal mechanisms, and a 0.25° × 0.25° stress field model. Our results reveal pronounced stress segmentation along the Longmenshan fault zone, driven by the interplay between regional tectonic compression and local fault geometry. Integrated analysis suggests that the structural complexity of the Dayi gap likely hinders gap-spanning ruptures. In contrast, the Zheduotang gap faces significantly elevated hazard due to persistent stress loading from the 2014 Kangding and 2022 Luding earthquakes. This unified high-resolution dataset provides a robust seismological framework for assessing geodynamic processes and future seismic risks in the region.

Keywords: Machine-learning, Earthquake, Focal mechanism, Stress field, Seismic gap

Key Points:

- A high-resolution dataset (2013-2022) with 180,000 relocated events and 2,524 focal mechanisms is developed via hybrid deep-learning strategies.
- Stress segmentation along the Longmenshan fault reveals that structural complexity within the Dayi gap likely hinders gap-spanning ruptures.

- The Zheduotang gap exhibits significantly elevated seismic hazard due to cumulative stress loading from the 2014 Kangding and 2022 Luding earthquakes.

1. Introduction

The Sichuan-Yunnan region (SYR) is situated at the eastern margin of the Tibetan Plateau (TP) and the south-central segment of the North-South Seismic Belt. Driven by the intense deformation from the India-Eurasia collision, the region is shaped by both the uplift of the TP and the eastward extrusion of crustal material. The SYR features complex geological structures (Figure 1a), characterized by a network of NW-, NE-, and nearly N-S-striking active fault zones (Zhang et al., 2003a; Zhang et al., 2005). These include major fast left-lateral strike-slip systems such as the Xianshuihe (XSH), Anninghe-Zemuhe (AZ), Xiaojiang (XJ), and Lijiang-Xiaojinhe (LX) faults; the predominantly thrusting Longmenshan fault (LMS) with a right-lateral component; and the right-lateral strike-slip Red River fault (RR). These large-scale fault systems subdivide the SYR into several active tectonic blocks, including the Songpan-Ganzi (SGB), Qiangtang (QTB), Sichuan-Yunnan (SYB), Sichuan Basin (SCB), Yunnan-Myanmar-Thailand (YMTB), and Indochina (ICB) blocks.

Intense tectonic deformation and block interactions facilitate stress accumulation along boundaries, resulting in complex fault systems that make the SYR one of the most seismically active regions in China, characterized by short recurrence intervals for strong earthquakes (Yi et al., 2002; Xu et al., 2005; Shao et al., 2025). Historically, M_S 6.0 events occurred frequently along the northwestern XSH, and the southern XJ. Since 2000, moderate-to-strong seismicity has shown a migration trend toward the LMS and

RR. Following the 2008 Wenchuan M_S 8.0 earthquake, the region has experienced a series of major events (Figure 1b), including the 2013 Lushan M_S 7.0, 2014 Ludian M_S 6.5, 2014 Kangding M_S 6.3, 2017 Jiuzhaigou M_S 7.0, 2019 Changning M_S 6.0 , 2021 Yangbi M_S 6.4, and 2022 Luding M_S 6.8 earthquakes. Furthermore, several unruptured seismic gaps along the LMS and the XSH-XJ remain areas of high concern and significant debate regarding their seismic hazard potential (Jiang & Zhuang, 2010; Wen et al., 2013; Guo et al., 2020; Zheng et al., 2024).

Current AI-driven seismic research in the SYR primarily targets localized faults or industrial sites. This leaves a critical gap for a systematic, regional-scale investigation encompassing the complete chain of seismic monitoring, focal mechanism determination, and stress field inversion. In this study, we integrate data from permanent and local seismic networks and employ advanced machine-learning techniques to systematically perform AI-based microseismic detection, relocation, focal mechanism solution (FMS) calculation, and regional stress inversion. Our objective is to construct a unified, high-precision catalog with a lower magnitude of completeness (M_C), a comprehensive FMS catalog, and a regional stress model based on 10 years of consistent data and methodology. This framework allows us to reveal the spatiotemporal evolution of tectonic activity, clarify the geodynamic origins of recent large earthquakes, and assess the seismic hazard of key fault zones.

The following sections first compare various AI-based microseismic detection algorithms and automated P-wave polarity picking methods. We then implement earthquake detection and relocation, extract waveforms for $M_L \geq 1.5$ events to calculate

FMS. Finally, we invert the regional stress field. These high-resolution results are utilized to delineate fine-scale fault geometry, analyze kinematic modes, and evaluate regional seismic potential.

2. Materials and Methods

2.1 Regional Networks and Data

We utilized three-component continuous data from 514 broadband seismic stations over a period of 10 years from 2013 to 2022, all recording with a sampling rate of 100 Hz. The network is composed of 101 permanent stations (blue triangles in Figure 1b) and 413 local stations (white triangles in Figure 1b). While the permanent network exhibits a relatively uniform spatial distribution with an average station spacing of 70 km. The integration of local arrays effectively reduces the average spacing to about 30 km within the SCB and along the LMS and AZ. In other major fault zones bordering the SYB, the the average spacing is approximately 45 km.

2.2 Comparison of Machine-Learning Phase-Pickers

We re-picked Pg and Sg phases for earthquake detection based on the permanent stations. Notably, 20% of phases in the manually-picked catalog (hereafter manual catalog) in the 2013 catalog exceed epicentral distances of 140 km (Figure S1), surpassing the training limits of conventional AI pickers. At such distances, head waves (Pn and Sn) precede direct waves (Pg and Sg), which can compromise picking accuracy and phase association. To address these large-scale challenges, we compare three AI-based methods: SAR (Zhou et al., 2025), PhaseNet+ (Zhu et al., 2025), and SKYNET(Aguilar-Suarez and Beroza, 2025).

① SAR (Self-Attention RNN) was trained on detections generated by PAL (Zhou et al., 2021), which combines the STA/LTA and Kurtosis algorithms for Pg and Sg phase picking. SAR enhances PAL's detection performance through training. In this study, we set the S-wave arrival window to 35 s, corresponding to a maximum distance of -300 km.

② PhaseNet+ simultaneously estimates phase arrivals and first-motion polarity (FMP). The model was trained using dataset from the Northern California Dense Network (NCEDC), with a maximum interstation distance of 140 km. For application in the Sichuan-Yunnan region, we applied a probability threshold of 0.3 for phase detection.

③ SKYNET is designed for regional-scale events (1°-20°), classifying among Pn, Pg, Sn, and Sg phases. It performes particularly well under conditions of sparse station coverage or seismicity lied outside the network. To complement distant phase picks beyond 140 km, we applied SKYNET with a higher probability threshold of 0.8.

We evaluated the three methods based on picking accuracy (Figure 2), error variation with epicentral distance (Figure S2), and the distribution of missed phases (Figure S3). PhaseNet+ exhibits the highest accuracy (with mean Pg and Sg errors of -0.01 s and -0.15 s, respectively) and the highest overall recall. Although absolute picking errors for all methods increase with epicentral distance, their growth rates vary: PhaseNet+ errors rise sharply beyond 100 km, whereas SKYNET shows a more gradual increase between 100 and 200 km. The distribution of missed phases underscores the influence of training ranges: 65% of phases missed by PhaseNet+ occur at distances >100 km, while 80% of those missed by SKYNET are at < 100 km, both falling outside their respective training limits.

To retain phases at distances exceeding 140 km and minimize interference from head waves, we developed a tailored picking strategy for the Sichuan-Yunnan region. First, PhaseNet+ is applied with a probability threshold of 0.3 to pick Pg and Sg phases. Subsequently, SKYNET is utilized with a threshold of 0.8 to supplement Pg and Sg arrivals at epicentral distances greater than 140 km. Following Aguilar-Suarez and Beroza (2025), we note that SKYNET's performance remains relatively stable across different probability thresholds.

2.3 Comparison of AI-based P-wave FMP Picking Methods

Following the AI-derived earthquake catalog, we extract event waveforms and determine the P-wave FMP for each event to constrain the FMS (Hardebeck and Shearer, 2002). Most current AI-based polarity picking methods rely heavily on precise arrival times. Given the arrival-time uncertainties inherent in PhaseNet+ picks (Figure S7a), it is necessary to account for the impact of these offsets on polarity identification. Therefore, we assessed three AI-based methods: PhaseNet+, RPNet (Han et al., 2025), and DiTingMotion (Zhao et al., 2023a).

① PhaseNet+, as described in section 2.2, simultaneously picked Pg arrivals along with FMP.

② RPNet integrated advanced deep-learning techniques for robust P-wave FMP determination, and was connected to the SKHASH algorithm (Skoumal et al., 2024) aimed at automated focal mechanism inversion. The model was trained on datasets from three different regions (SCEDC, PNW, and INSTANCE). In order to improve the accuracy in the case of P-wave arrivals with deviation, dense random time shifts were applied during training.

③ DiTingMotion was trained on a hybrid dataset combining DiTing (Zhao et al., 2022) with the SCSN-FMP (Ross et al., 2018b). This method has been widely applied across mainland China for automatic FMP determination and provided associated confidence metrics indicating clarity.

With accurate P-wave arrival times, RPNet achieves over 90% accuracy for both up and down polarities, outperforming DiTingMotion (Figure 3, top row). When using arrival times predicted by PhaseNet+, RPNet's performance shows negligible degradation and remains superior to both DiTingMotion and PhaseNet+ (Figure 3, bottom row). In contrast, DiTingMotion's accuracy drops by approximately 10% compared to the accurate-timing scenario. Overall, RPNet's stability and high accuracy (> 90%) in both cases make it ideal for our workflow.

Further analysis of misidentified polarities (False U_D, U_K, D_U, and D_K) reveals weak correlations with epicentral distance and magnitude (Figures S4 and S5). Instead, errors are concentrated at specific stations with low signal-to-noise ratios. This suggests that polarity picking accuracy is largely independent of earthquake size or distance, but rather depends on data quality at individual stations

3. Results

3.1 Earthquake Detection and Relocation

An earthquake catalog was built by applying five publicly available packages to three-component waveform data from 101 permanent stations in the Sichuan-Yunnan region, spanning a decade from 2013 to(2022). The workflow integrated PhaseNet+ and SKYNET for seismic phase picking, the PAL for association and preliminary location, Hypoinverse (Klein, 2002) for absolute location, and 3D-HypoDD (Waldhauser & Ellsworth, 2000) for relocation.

Initially, utilizing the phase picking strategy described in Section 2.2, we identified 5 million Pg phases and 4.1 million Sg phases. In the second stage, the PAL was employed for temporal clustering of origin times followed by spatial association via a 3D grid search. The association criteria required at least four stations with an original time deviation < 1.5 s. A total of 79,579 earthquakes were detected (including 516,492 Pg and 477,734 Sg phases), whereas the manual catalog for the same period recorded 60,308 events. The spatial distribution of the PAL-associated catalog is consistent with the manual catalog, showing concentrations along major active faults and plate boundaries. Notably, the AI-based detection increased the number of small-magnitude events ($M_L < 2.0$), effectively reducing the M_C from 2.5 to 2.2 (Figure S6). The focal depths of the associated results exhibit a bimodal distribution, peaking at 5 km and 15 km.

To maximize data utility and enhance location accuracy, the relocation phase integrated AI detections from permanent stations with manual phase reports from local stations. For the Hypoinverse absolute location, a 1D velocity model was derived by regionally averaging the 3D CSES velocity model (Wu et al., 2024) across the study area at 4-km depth intervals. For HypoDD relocation, we utilized only travel-time data and the 3D CSES model with a horizontal resolution of 0.25° × 0.25°. Detailed uncertainties and errors associated with the picking and location processes are discussed in Section 4.1.

The final high-precision catalog (hereafter AI catalog) contains 180,000 earthquakes. While its overall spatial pattern remains consistent with the initial detections and the manual catalog, it provides a more refined characterization of major fault structures (Figure 4a). Focusing on the seismicity characteristics of major active faults, moderate-to-strong earthquake sequences, and typical energy exploitation areas, we subdivided the study region into five sub-regions (blue polygons in Figure 4a).

C1 LMS: Compared to the manual catalog, the AI catalog reveals clearer seismicity segmentation and depth structures (Figure 5 and Figure S10). The front segment (L1) hosted the 2013 Lushan M_S7.0 earthquake, with a prominent seismic gap between it and the central segment (L2). Its rupture risk is detailed in Section 4.3.1. The L2 exhibits the highest seismicity level. Along the SW-NE striking main fault, focal depths migrate downward over time (Figure 5 C1-C2 and D1-D2), leaving a 0-10 km seismic gap (Figure 5 A1-A2). On the NW-SE striking conjugate faults, seismicity clusters above 10 km and deepens to 20 km as it approaches the main fault (Figure 5 B1-B2). In the back-range segment (L3) shows significantly reduced activity, with focal depths deepening northeastward along the strike. Compared to the L2, the L3 features narrower seismic belts, steeper dips, and a near-vertical geometry (Figure 5 F1-F2 and G1-G2).

C2 Intersection area of XSH, AZ, and LMS: This region hosted the 2022 Luding M_S 6.8 earthquake following the 2014 Kangding M_S 6.3 earthquake, leaving a seismic gap between them (Figure 6); its potential hazard is detailed in Section 4.3.2. The AI catalog reveals clearer linear structures and N-S depth variations. Specifically, XSH focal depths remain shallower than 15 km and shallow southeastward along the strike (Figure 6 A1-A2). Seismicity along the AZ exhibits a bifurcated structure extending to 30 km with marked lateral heterogeneity with deeper events occurring on the eastern side. Additionally, focal depths in both faults exhibit a downward migration over time (Figure 6 D1-D2).

C3 Intersection area of RR and LX: Seismicity along the RR and its branches exhibits distinct clustering and a southeastward migration trend (Figure 7ab). The AI catalog further reveals NNE-SSW secondary faults situated between multiple parallel NW-SE striking main faults.

C4 Intersection area of the northern XJ and AZ: The AI catalog refines the seismic depth distribution in this region (Figure 7cd and Figure S10). To the east, the L-shaped cluster representing the 2014 Ludian M_S 6.5 sequence shows focal depths shallowing westward over time. To the west, the Y-shaped cluster corresponds to Baihetan reservoir-induced seismicity, concentrated after the 2021 impoundment. Regarding the Y-shaped structure, the AI catalog corrects the manual interpretation that the main trunk was shallower than the branches. It identifies the eastern branch as the deepest (10-15 km), whereas the western branch and main trunk are shallower (< 10 km), and the central junction is the shallowest (< 5 km).

C5 Shale gas field in SCB: Seismicity is concentrated around hydraulic fracturing platforms in the Weiyuan (Lei et al., 2019) and Changning (Lei Xinglin et al., 2020; Zhang et al., 2024) fields, characterized by dense spatial clustering (Figure 7e). These seismic clusters exhibit a strong spatiotemporal correlation with hydraulic fracturing stages (Figure 7f).

3.2 Small-to-Moderate Earthquakes Focal Mechanisms

We extracted waveforms for events with $M_L > 1.5$ from the AI catalog and determined P-wave FMP and S/P amplitude ratios using the RPNet method described in Section 2.3. FMS for small-to-moderate earthquakes were subsequently calculated using the SKHASH program. We required at least eight P-wave polarity, a maximum epicentral distance of 200 km, an azimuthal gap of less than 90°, and a takeoff angle gap of less than 60°. This process yielded FMP for 15,000 earthquakes and their uncertainties. Following the quality classification criteria of Hardebeck and Shearer (2003), 2,524 solutions categorized as Class A and B were selected for further analysis (Table S1, Figure S11). A detailed discussion of uncertainty estimation and quality filtering is provided in Section 4.1.

Within our FMS catalog, magnitudes are primarily concentrated between M_L 2.0 and 4.0 (2,211 events), while moderate-to-strong earthquakes ($M_L \geq 5.0$) account for only 1.5% (37 events). Given the inherent limitations of polarity-based methods in stably and accurately resolving larger events (Zhu & Ben-Zion, 2013), we refined the solutions for $M_L \geq 5.0$ events. Specifically, results for M_L 5.0-6.0 events were substituted with waveform inversion results from Guo et al. (2025), and events exceeding M_L 6.0 were updated with Global Centroid Moment Tensor (GCMT) solutions (Figure S13).

FMS were classified based on the surface strain derived from horizontal strain flower theory (Table S2; Wan, 2024). The study area is dominated by strike-slip types

(52.46%), followed by thrust fault types (15.10%), normal fault types (9.27%), thrust fault with strike-slip components (12.40%), and normal fault with strike-slip components (10.78%). The spatial distribution of these mechanisms delineates the distinct kinematic modes of major fault zones (Figure 8a). The main LMS is characterized by thrusting, while the XSH, XJ and RR predominantly exhibit strike-slip motion. Due to the susceptibility of small-magnitude FMS to structural complexity, focal types become more heterogeneous at fault intersections. For instance, both strike-slip and normal faulting coexist along conjugate faults in the central segment of the LMS. Additionally, at the eastern boundary of the SYB, localized normal and thrust faulting occur in response to secondary block extension or compression induced by differential slip rates.

3.3 Regional Stress Field Model

We further inverted the crustal tectonic stress field based on the FMS catalog. A linear damped inversion method (Hardebeck & Michael, 2006) was employed to characterize the regional stress field, while the StressInverse method (Vavryčuk, 2014) was used to calculate the average compressive stress axes and stress ratios for major active faults. Based on the density and distribution of the FMS, the study area was discretized into a 0.25° × 0.25° grid. For each grid node, all events within a 25-km radius were included in the stress tensor inversion, provided that at least five focal mechanisms were available. The damping parameter $e = 2.75$. The uncertainties of the inversion results and the impact of grid size are discussed in detail in Section 4.1.

Consistent with the kinematic patterns revealed by the focal mechanisms, the stress field around the LMS is characterized by horizontal compression. In contrast, the XSH, XJ and RR generally exhibit strike-slip stress regimes, with localized horizontal extension observed at the northern segment of the XJ and the intersection of the RR and LX (Figure 8b). On a regional scale, the principal stress orientations exhibit a prominent clockwise rotation along the eastern boundary of the SYB. The principal compressive stress (σ1) shifts from NW-SE compression at the SGB-SYB boundary to NNW-SSE at the junction of the SYB- SC-ICB, and further rotates to a nearly N-S direction at the SYB-ICB boundary. This clockwise rotation is also reflected in the average stress orientations of the major faults: 108° for the XSH (X1), 120° for the AZ (X2), and 128° for the northern XJ (X3). Furthermore, the average stress ratio increases from 0.713 at the XSH to 0.941 at the XJ, indicating a southward transition from a compression-dominated to an extension-influenced regime.

At a local scale, the LMS exhibits a more complex stress structure (Figure 9a-d). First, the stress regime displays distinct depth-dependent segmentation: the L1 shows a strike-slip regime at 10 km depth but shifts to a compression-dominated regime at 15-25 km; the L2 features strike-slip stress across its conjugate faults at all depths, while the main fault transitions to compression at 15 km depth; the L3 maintains a compressive stress regime throughout the investigated depth range. Additionally, the σ1 orientation also exhibits segmentation, with NWW-SEE compression in the L1 and L2 aligning with the regional tectonic field. Notably, we observed a depth-dependent variation of σ1 in the L3: between 10 and 15 km, the angle between the σ1 axis and the fault strike gradually increases until they are nearly perpendicular; at 20 km, the σ1 orientation on the northern side of the fault shows a counter-clockwise rotation; and at 25 km, the angle decreases again, with σ1 becoming nearly parallel to the fault strike.

4. Discussion

4.1 Model Quality Control and Reliability Verification

We demonstrate the feasibility of applying deep-learning workflows to the SYR and validate the reliability of our AI catalog, FMS catalog, and regional stress model through two primary lines of evidence.

First, we implemented rigorous parameter thresholds with quantifiable uncertainties and errors at every stage. In seismic detection, Pg and Sg picks exhibit minimal delays compared to manual reports, with mean deviations of 0.02 s and 0.15 s, and mean probabilities of 0.73 and 0.60, respectively (Figure S7). Recall rates for Pg, Sg, and earthquake events reach 87.34%, 77.01%, and 90.17%. During phase association, Pg and Sg travel times show excellent fits with average velocities of 5.98 km/s and 3.45 km/s; the absence of downward curvature beyond 150 km epicentral distances indicates no contamination from Pn and Sn phases (Figures S8, S9). The average relocation error reported by hypoDD is 83.15 m in the horizontal direction and 129.94 m in the vertical direction, with a root-mean-square (RMS) travel-time residual of 0.11 s, retaining 80.47% of detected events. For P-wave FMP, the mean picking probability is 94.03%. Quality analysis shows that Class C and D FMS are primarily driven by data insufficiency rather than algorithmic limitations (Figure S11). The Class A and B solutions used for analysis are constrained by an average of 12 Pg polarities, with average polarity misfit of 0.11, mean plane uncertainty of19°, station distribution ratio of 0.67, and a best-fit probability of 85% (Figure S12). In stress inversion, the mean maximum errors for the three principal stress axes are 18.15°, 39.11°, and 13.57°, with a mean error of 0.012 for the stress ratio.

Furthermore, our results show high consistency with published findings. The AI catalog delineates linear seismicity along major fault zones and clusters in industrial injection-extraction areas, correlating with velocity anomalies in regional models (Liu et al., 2021; Wu et al., 2024). Aftershock sequences in the AI catalog align with high-resolution relocations from temporary arrays, such as the Y-shaped structure of the 2013 Lushan earthquake (Fang et al., 2015), the L-shaped conjugate faults of the 2014 Ludian earthquake (Fang et al., 2014), and the NW-NE en-echelon structures of the 2021 Yangbi earthquake (Su et al., 2021; Lei et al., 2021; Duan et al., 2021). Our FMS catalog captures fault kinematics consistent with waveform inversions of moderate-to-strong historical events (Guo et al., 2025) while significantly expanding the sample size for M_L 1.5-4.0 events. The accuracy of these small-event solutions is corroborated by studies on seismogenic structures (Luo et al., 2019) and regional stress (Duan et al., 2019; Tian et al., 2019). Our regional stress field model, inverted on a 0.25° × 0.25° grid, matches the orientations reported by studies using coarser 0.3° - 2° grids (Xu et al., 2016; Zhang et al., 2022; Tian et al., 2025). The large-scale clockwise rotation of principal stresses along the eastern boundary of the SYB is cross-validated by in-situ stress measurements (Xie et al., 2007) and GPS strain fields (Fu et al., 2025). Notably, by extending the magnitude threshold to $M_L \geq 1.5$, the increased spatial sampling density reveals a novel feature: depth-dependent stress rotation within the LMS.

4.2 Longmenshan Fault Zones: Segmented Stress Field and Tectonic Control Mechanisms

As detailed in Section 3.3, stress regimes and σ1 orientations exhibit pronounced spatial heterogeneity along the LMS. This complex southwest-to-northeast segmentation pattern is corroborated by multiple investigations of tectonic stress fields and seismic anisotropy. Specifically, the high-resolution (0.1° × 0.1°) post-seismic stress field (2008-2010) inverted by Luo (2019) and the long-term stress field (1970-2021) reported by Tian (2025) reveal consistent segmented stress structures. Furthermore, seismic anisotropy studies indicate that fast shear-wave polarization and Pms-wave fast directions undergo a SW-NE transition from NWW to NW/NE, and then revert to NWW/NE (Zhang et al., 2018; Chen et al., 2019).

Quantitative comparisons by Tian (2025) between fast-wave directions and σ1 orientations show strong alignment in L1, reflecting a tectonic-dominated deformation regime. In contrast, significant discrepancies occur at the L2-L3 boundary, suggesting multi-factor control in this region. Absolute stress analysis at equivalent depths reveals a decrease in normal stress and an increase in shear stress from L1 to L3 (Li et al., 2022), accompanied by a gradual reduction in σ1 (Su et al., 2025). Correspondingly, crustal shortening rates (Chen et al., 2005) and surface uplift (Pan et al., 2018) in L1 are higher than those in L3. These observations suggest that the stress field in L1 is primarily driven by the convergence between the SGB and the SCB, whereas the influence of this compression weakens toward L2 and L3. Our study further identifies a local stress anomaly at the L2-L3 transition: at depths shallower than 20 km, the σ1 orientation rotates to NE-SW (Figure 9c) with a corresponding jump in σ1 value (Su et al., 2025). Considering the geometry and depth constraints (< 20 km) of the NNE-striking branch faults in the Minshan Uplift (Tan et al., 2010; Lu et al., 2022), we conclude that the stress segmentation and rotation are the combined result of regional compression and shallow block-bounding faulting.

4.3 Seismic Gaps: Differential Risk Revealed by Multi-Parameter Evidence

4.3.1 Dayi Seismic Gap in Longmenshan Fault Zones

A 40-60 km rupture gap, known as the Dayi seismic gap, exists between the 2013 Lushan and 2008 Wenchuan earthquakes along the LMS. Its seismic hazard has attracted significant attention and remains a subject of intense debate (Zheng et al., 2024). P- and S-wave velocity tomographies reveal a consistent low-velocity anomaly throughout the upper and lower crust within the gap, suggesting a weak medium that is unfavorable for strain energy accumulation (Wang et al., 2015; Pei et al., 2019). Conversely, investigations of kinematic and stress states suggest the region is in an interseismic stage of high stress accumulation, with a heightened potential for a full-gap rupture. For instance, GNSS interseismic velocity fields (Zhao et al., 2020) and post-seismic afterslip models of the Wenchuan earthquake (Diao et al., 2018) indicate significant slip deficits and strain accumulation. Furthermore, in-situ stress measurements via hydraulic fracturing across the Shuangshi-Dachuan fault reveal high-stress conditions (Li, 2021), while both coseismic and post-seismic Coulomb stress changes from the Wenchuan and Lushan events have positively loaded the gap, further promoting potential failure (Guo et al., 2020).

In this study, the spatial distribution of b-values along the LMS, calculated from an AI catalog, reveals relatively low b-values on both flanks of the gap (Figure 9e). This is consistent with the hypothesis of regional stress concentration. However, regional stress field analysis demonstrates distinct stress regimes and σ1 orientations on either side of the gap (Figure 9f). The Lushan source area to the west is dominated by a compressional regime with σ1 oriented NW-SE (perpendicular to the fault strike). To the east, the strike-slip component increases as the angle between σ1and the fault strike gradually decreases, likely due to differential sliding across multiple parallel faults acting as block boundaries. These inconsistent stress structures suggest a high degree of rupture complexity that may limit the development of a sustained rupture system. Paleoseismological evidence further supports the characteristic of segmented rupture within the gap (Wang et al., 2015); for example, the 1970 M_S 6.2 earthquake in the southeastern portion exhibited a limited rupture length of less than 20 km (Li et al., 2017). Consequently, considering the complexity of the rupture system, the Dayi seismic gap is less prone to a gap-spanning earthquake.

4.3.2 Zheduotang Fault Seismic Gap in Xianshuihe Fault Zones

In the southern XSH, the Zheduotang seismic gap—situated between the 2014 Kangding and 2022 Luding ruptures—presents a critical seismic hazard, particularly as it intersects the Sichuan-Tibet Railway (Figure 10a). High shallow locking in this segment is well-documented: geodetic data (GNSS and InSAR) reveal a distinct southward "deceleration-acceleration" slip-rate profile (Figure 10b), with the Zheduotang segment exhibiting a localized slip deficit (3-4.8 mm/a) compared to the adjacent Selaha and Moxi segments (Zhou et al., 2001; Li et al., 2020). Interseismic models confirm this, showing locking coefficients of 0.6-1.0 and a seismic asperity at 0-10 km depth (Jiang, 2015b; Zhu et al., 2024). Given the XSH exhibits consistent strike-slip regime, a full-gap rupture would likely cause severe surface shear damage.

Our analysis confirms that both the 2014 Kangding and 2022 Luding earthquakes significantly intensified the hazard within this gap. Following these earthquakes, seismicity within the gap vicinity markedly increased (Figure 10e). And b-values remained persistently low in the periods both before and after the 2022 Luding earthquake (Figures 10bc), suggesting a sustained state of high stress concentration within the gap. Furthermore, coseismic Coulomb failure stress change indicate that the Zheduotang segment was positively loaded by both the Kangding (Figure 10d) and Luding earthquakes (Zhao et al., 2023). In summary, the Zheduotang fault possesses high intrinsic seismogenic potential, and successive stress loading from recent strong earthquakes has further elevated the risk of a major rupture.

5. Conclusions

We developed a hybrid AI-based framework for large-scale seismic monitoring, providing a high-resolution characterization of seismicity and geodynamics in the Sichuan-Yunnan region (2013-2022). The key findings are:

(1) Methodological Efficiency: The hybrid AI strategy significantly enhanced phase recall (Pg from 82.57% to 87.34%, Sg from 65.03% to 77.01%) and achieved > 90% accuracy in first-motion polarity picking for small-to-moderate earthquakes, ensuring a robust foundation for regional-scale catalogs.

(2) High-Resolution Datasets: Our 10-year relocated catalog comprises -180,000 events, with the magnitude of completeness improved to 2.2. A new database of 2,524 focal mechanisms (M_L 2.0-4.0) and a 0.25° × 0.25° stress field model reveal intricate fault geometries and complex rupture patterns at fault junctions.

(3) Stress Heterogeneity: The Longmenshan Fault Zone is not a uniform stress unit but exhibits pronounced segmentation. While the mountain-front segment is dominated by Songpan-Ganzi block and Sichuan basin convergence, the central-to-back range transition is modulated by NNE-striking branch faults, causing stress regime rotations and $\sigma1$ deviations at depths < 20 km.

(4) Differentiated Gap Hazards: The Dayi gap, despite being locked, is unlikely to host a gap-spanning rupture due to its complex, segmented architecture. Conversely, the Zheduotang gap exhibits high seismogenic potential, with its hazard further elevated by successive stress loading from the 2014 Kangding and 2022 Luding earthquakes.

Acknowledgements

We thank Prof. Yue Han, Prof. Jia Ke, Prof. Zhang Heng and Dr. Tian Jianhui for suggestive discussion. This study was jointly funded by the National Key R&D Program (2025YFB3003604), Key Science and Technology Project of Ministry of Emergency Management of the People’s Republic of China (2025EMST040201), the National Natural Science Foundation of China (Grant No. U2539201, 42174066, 42474089) and the Fundamental Research Funds of the Institute of Earthquake Forecasting, China Earthquake Administration (Grant Nos. CEAIEF20240405).

Data and Resources

The three-component waveform data involved in this study was provided by the China Earthquake Networks Center (https://www.cenc.ac.cn/). The relocation catalog, focal mechanisms catalog and stress field model are available from the author. The supplemental material accompanying this article includes details of the quality assessment, as well as a comparison with the manual catalog.

Declaration of Competing Interests

The authors declare that they have no conflict of interest.

References

Aguilar-Suare, A. L., and G. Beroza (2025). Picking regional seismic phase arrival times with deep learning, *Seismica* **4**, no. 1, https://doi.org/10.26443/seismica.v4i1.1431.

Bai, M. K., M. Chevalier, P. H. Leloup, H. B. Li, J. W. Pan, A. Replumaz, *et al.* (2021). Spatial slip rate distribution along the SE Xianshuihe fault, eastern Tibet, and earthquake hazard assessment, *Tectonics* **40**, no. 11, e2021TC006985.

Chen, A. G., Y. Gao, and Y. T. Shi (2019). Seismic anisotropy and its variation in the upper crust beneath the Longmenshan fault zone, *Chinese Journal of Geophysics* **62**, no. 8, 2959-2981.

Chen, Z. X., D. Jia, Q. Zhang, G. Q. Wei, B. L. Li, D. T. Wei, *et al.* (2005). Balanced cross-section analysis of the fold-thrust belt of the Longmen Mountains, *Acta Geologica Sinica* **79**, no. 1, 38-45.

Diao, F. Q., R. J. Wang, Y. B. Wang, X. Xiong, and T. R. Walter (2018). Fault behavior and lower crustal rheology inferred from the first seven years of postseismic GPS data after the 2008 Wenchuan earthquake, *Earth and Planetary Science Letters* **495**, 202-212.

Duan, M. Q., C. P. Zhao, L. Q. Zhou, C. Zhao, and K. Z. Zuo (2021). Seismogenic structure of the 21 May 2021 MS6.4 Yunnan Yangbi earthquake sequence (in Chinese), *Chinese Journal of Geophysics* **64**, no. 9, 3111-3125.

Duan, M. Q., L. Q. Zhou, L. F. Duan, Z. Y. Li, C. P. Zhao, ang X. D. Zhang (2024). Earthquake migration characteristics and triggering mechanisms in the Baihetan reservoir area based on machine-learning microseismic detection, *Geophysical Journal International* **239**, no. 3, 1650-1663.

Duan, L. F., C. P. Zhao, L. Q. Zhou, C. Zhao, W. Guo, M. Q. Duan, K. Z. Zuo, and L. S. Xu (2025).

Unraveling the dynamics of seismicity in the Baihetan Reservoir Area with AI-based catalog, *Tectonophysics* **896**, 230601.

Fang, L. H., J. P. Wu, W. L. Wang, Z. Y. Lu, C. Z. Wang, T. Yang, and S. J. Zhong (2014). Relocation of the aftershock sequence of the MS 6.5 Ludian earthquake and its seismogenic structure (in Chinese). *Seismology and Geology* **36**, no. 4, 1173-1185.

Fang, L. H., J. P. Wu, W. L. Wang, W. K. Du, J. R. Su, C. Z. Wang, et al. (2015). Aftershock observation and analysis of the 2013 MS 7.0 Lushan earthquake, *Seismological Research Letters* **86**, no. 4, 1135-1142.

Feng, T., R. J. Wang, L. H. Fang, J. P. Wu, and T. Yang (2024). Microseismic constraints on the mechanical state of the Anninghe-Daliangshan fault zone, southeastern Tibetan Plateau, *Earth and Planetary Science Letters* **639**, 118765.

Fu, Z., X. Zhang, X. Y. Guo, H. Liu, and Y. Zhou (2025). The three-dimensional spatial distribution characteristics of tectonic stress field in the Sichuan-Yunnan region (in Chinese), *Chinese Journal of Geophysics* **68**, no. 7, 2498-2514.

Guo, R. M., Y. Zheng, J. Q. Xu (2020). Stress modulation of the seismic gap between the 2008 MS 8.0 Wenchuan earthquake and the 2013 MS 7.0 Lushan earthquake and implications for seismic hazard, *Geophysical Journal International* **221**, 2113-2125.

Guo, C., J. L. Li, W. W. Wu (2025). A new-generation source mechanism catalogue for historical moderate-to-strong earthquakes in the Sichuan-Yunnan region constrained by a topographic high-resolution 3D velocity model and seismic waveform matching, *Science China Earth Sciences* **68**, 4139-4162.

Hardebeck, J. L. and A. J. Michael 2006. Damped regional-scale stress inversions: Methodology and examples for southern California and the Coalinga aftershock sequence, *Journal of Geophysical Research: Solid Earth* **111**, B11310.

Han, J., S. Kim, and D. H. Sheen (2025). RPNet: Robust P-Wave first-motion polarity determination using deep learning, *Seismological Research Letters* **96**, no. 4, 2405-2417.

Jiang, C. S. and J. C. Zhuang (2010). Evaluation of background seismicity and potential source zones of strong earthquakes in the Sichuan-Yunan region based on the space-time ETAS model, *Chinese Journal of Geophysics* **53**, no. 2, 305-317.

Jiang, G. Y., X. W. Xu, G. H. Chen, Y. J. Liu, Y. Fukahata, H. Wang (2015b). Geodetic imaging of potential seismogenic asperities on the Xianshuihe-Anninghe-Zemuhe fault system, southwest China, with a new 3-D viscoelastic interseismic coupling model, *Journal of Geophysical Research: Solid Earth* **120**, 1855-1873.

Klein, F. W. (2002). User's Guide to HYPOINVERSE-2000, a Fortran Program to Solve for Earthquake Locations and Magnitudes 4/2002 version, *United States Department of the Interior Geological Survey*, 2002-171, doi: 10.3133/ofr02171.

Lei, X. L., Z. W. Wang, and J. R. Su (2019b). Possible link between long-term and short-term water injections and earthquakes in salt mine and shale gas site in Changning, south Sichuan Basin, China, *Earth and Planetary Physics* **3**, 510-525.

Li, B., F. R. Xie, J. S. Huang, X. W. Xu, Q. L. Guo, G. W. Zhang, *et al.* (2022). In situ stress state and seismic hazard in the Dayi seismic gap of the Longmenshan thrust belt, *Science China Earth Sciences* **65**, no. 7, 1388-1398.

Li, J. G., B. G. Zhou, T. M. Li, Y. L. Yang, and Z. F. Li (2020). Locking depth, slip rate, and seismicity distribution along the Daofu-Kangding segment of the Xianshuihe fault system, eastern Tibetan Plateau, *Journal of Asian Earth Sciences* **193**, no. 15, 104328.

Li, J. L., J. Xu, H. J. Zhang, W. Yang, Y. Y. Tan, F. S. Zhou, *et al.* (2023). High seismic velocity structures control moderate to strong induced earthquake behaviors by shale gas development. *Communications Earth and Environment* **4**, 188.

Li, Y. C., J. M. Nocquet, X. J. Shan, and H. Z. Jian (2021). Heterogeneous interseismic coupling along the Xianshuihe-Xiaojiang fault system, eastern Tibet, *Journal of Geophysical Research: Solid Earth* **126**, e2020JB021187.

Li, Y., Y. F. Cui, Z. F. Li, and X. Fu (2022). Evolution of Glacier Debris Flow and Its Monitoring System along Sichuan-Tibet Traffic Corridor (in Chinese), *Earth Science* **47**, no. 6, 1969-1984.

Li, Z. G., J. Liu-Zeng, R. Almeida, J. Hubbard, C. Sun, and G. X. Yi (2017). Re-evaluating seismic hazard along the southern Longmen Shan, China: Insights from the 1970 Dayi and 2013 Lushan earthquakes, *Tectonophysics* **717**, 519-530.

Li, Z. Y., L. Q. Zhou, M. Q. Duan, and C. P. Zhao (2024). Deep learning-based microseismic detection and location reveal the seismic characteristics and causes in the Xiluodu reservoir, China, *Bulletin of the Seismological Society of America* **114**, 806-822.

Liu, Y., Z. Y. Yu, Z. Q. Zhang, H. J. Yao, W. T. Wang, H. J. Zhang, H. F. Yang, and L. H. Fang (2023). The high-resolution community velocity model V2.0 of southwest China, constructed by joint body and surface wave tomography of data recorded at temporary dense arrays, *Science China Earth Sciences* **66**, 2368-2385.

Luo, Y., L. Zhao, and J. H. Tian (2019). Spatial and temporal variations of stress field in the Longmenshan fault zone after the 2008 Wenchuan, China earthquake, *Tectonophysics* **767**, 228172.

Lu, R. Q., Y. D. Liu, X. W. Xu, X. Tan, D. He, G. Yu, *et al.* (2019). Three-dimensional model of the lithospheric structure under the eastern Tibetan Plateau: Implications for the active tectonics and seismic hazards, *Tectonics* **38**, 1292-1307.

Martínez-Garzón, P., M. A. Meier, C. Collettini, F. Lanza, and G. Dresen (2025). Stress heterogeneities governed by fault structure and stress transfer: The 2016-2017 central Italy seismic sequence, *Journal of Geophysical Research: Solid Earth* **130**, e2024JB029763.

Meier, M. A., F. Lanza, P. Martínez-Garzón, and L. Chiaraluce (2025). Insights into extensional tectonics from a large deep learning focal mechanism catalog, *Bulletin of the Seismological Society of America* **115**, no. 6, 2690-2704.

Pan, Y. J., W. B. Shen, and C. K. Shum (2018). Spatially varying surface seasonal oscillations and 3-D crustal deformation of the Tibetan Plateau derived from GPS and GRACE data, *Earth and Planetary Science Letters* **502**, 12-22.

Pei, S. P., F. L. Niu, Y. Ben-Zion, Q. Sun, Y. B. Liu, X. T. Xue, J. R. Su, and Z. G. Shao (2019). Seismic velocity reduction and accelerated recovery due to earthquakes on the Longmenshan fault, *Nature Geoscience* **12**, 387-392.

Ross, Z. E., M. A. Meier, and E. Hauksson (2018b). P wave arrival picking and first-motion polarity determination with deep learning, *Journal of Geophysical Research: Solid Earth* **123**, no. 6, 5120-5129.

Sibson, R. (1985). Stopping of earthquake ruptures at dilutional fault jogs, *Nature* **316**, no. 6025, 248-251, doi: 10.1038/316248a0.

Shao, Z. G., W. X. Wang, Q. Liu, A. X. Dou, X. Q. Wang, Y. Q. Wu, *et al.* (2025). Study on the prediction of seismic hazard and seismic risk assessment for the next 10 years in the Chinese mainland (in Chinese), *Earthquake* **45**, no. 3, 193-218.

Skoumal, R., J. Hardebeck, and P. M. Shearer (2024). SKHASH: A python package for computing earthquake focal mechanism, *Seismological Research Letters* **95**, 2519-2526.

Su, J. B., M. Liu, Y. P. Zhang, W. T. Wang, H. Y. Li, J. Yang, *et al.* (2021). High resolution earthquake catalog building for the 21 May 2021 Yangbi, Yunnan, MS6.4 earthquake sequence using deep-learning phase picker (in Chinese), *Chinese Journal of Geophysics* **64**, no. 8, 2647-2656.

Su, P. Z., Y. Luo, and L. Zhao (2025). Three-dimensional crustal stress model construction for the Sichuan-Yunnan region (in Chinese), *Chinese Journal of Geophysics* **68**, no. 5, 1730-1750.

Tan, Y. Y., J. W. Qian, J. Hu, H. J. Zhang, H. L. Xing, J. L. Li, *et al.* (2023). Tomographic evidences for hydraulic fracturing induced seismicity in the Changning shale gas field, southern Sichuan Basin, China, *Earth and Planetary Science Letters* **605**, 118021.

Tian, J. H., Y. Luo, and L. Zhao (2019). Regional stress field in Yunnan revealed by the focal mechanisms of moderate and small earthquakes, *Earth and Planetary Physics* **3**, no. 2, 1-10.

Tian, J. H., and Y. Gao (2025). Present-day stress field in SE margin of Tibetan plateau by comprehensive updated earthquake focal mechanisms and its tectonic implications, *Tectonophysics* **910**, 230817.

Vavrycuk, V. (2014). Iterative joint inversion for stress and fault orientations from focal mechanisms, *Geophysical Journal International* **199**, no. 1, 69-77.

Waldhauser, F. and W. L. Ellsworth (2000). A double-difference earthquake location algorithm: method and application to the northern Hayward fault, California, *Bulletin of the Seismological Society of America* **90**, 1353-1368.

Wan, Y. G. (2024). Focal mechanism classification based on areal strain of horizontal strain rosette of focal mechanism and characteristic analysis of overall focal mechanism of earthquake sequence, *Earth Science* **49**, no. 7, 2675-2684.

Wang, F., M. Wang, Y. Z Wang, and Z. K. Shen (2015). Earthquake potential of the Sichuan-Yunnan region, western China, *Journal of Asian Earth Sciences* **107**, 232-243.

Wang, Z., J. R. Su, C. X. Liu, and X. L. Cai (2015). New insights into the generation of the 2013 Lushan Earthquake (MS7.0), China, *Journal of Geophysical Research: Solid Earth* **120**, 3507-3526.

Wang, M. and Z. K. Shen (2020). Present-day crustal deformation of continental China derived from GPS and its tectonic implications, *Journal of Geophysical Research: Solid Earth* **125**, no. 2, e2019JB018774.

Wu, J. P., Y. Cai, W. Wang, W. L. Wang, L. H. Fang, Y. N. Liu, and J. Liu (2024). Three-dimensional velocity model and its tectonic implications at China Seismic Experimental Site, eastern margin of the Tibetan Plateau, *Science China Earth Sciences* **67**, 2268-2290.

Xie, F. R., Q. C. Chen, X. F. Cui, H. Li, S. X. Yang, Q. L. Guo, *et al.* (2007). Fundamental database of crustal stress environment in continental China (in Chinese), *Progress in Geophysics* **22**, no. 1, 131-136.

Xu, X. W., P. Z. Zhang, X. Z. Wen, Z. L. Qin, G. H. Chen, and A. L. Zhu (2005). Features of active tectonics and recurrence behaviors of strong earthquakes in the western Sichuan province and its adjacent region (in Chinese), *Seismology and Geology* **27**, no. 3, 446-461.

Xu, Z. G., Z. C. Huang, L. S. Wang, M. J. Xu, Z. F. Ding, P. Wang, *et al.* (2016). Crustal stress field in Yunnan: implication for crust-mantle coupling, *Earthquake Science* **29**, no. 2, 105-115.

Yang, Y. H., X. M. Zhang, Q. Hua, L. N. Su, C. J. Feng, Y. R. Qiu, *et al.* (2021). Segmentation characteristics of the Longmenshan fault-constrained from dense focal mechanism data, *Chinese Journal of Geophysics* **64**, no. 4, 1181-1205.

Yi, G. X., X. Z. Wen, and X. W. Xu (2002). Study on recurrence behaviors of strong earthquakes for several entireties of active fault zones in Sichuan-Yunnan region (in Chinese), *Earthquake Research in China* **18**, no. 3, 267-276.

Zhang, G. M., H. S. Ma, H. Wang, and X. L. Wang (2005). Boundaries between active_tectonic blocks and strong earthquakes in the China mainland (in Chinese), *Chinese Journal of*

Geophysics **48**, no. 3, 602-610.

Zhang, N., L. Q. Zhou, M. Q. Duan, Z. P. Wen, and Q. J. Wu (2024). The temporal and spatial evolution characteristics of induced seismicity in the Changning shale gas field based on dense array, *Scientific Reports* **14**, 25287.

Zhang, P. Z., Q. D. Deng, G. M. Zhang, J. Ma, W. J. Gan, W. Min, F. Y. Mao, and Q. Wang (2003). Active tectonic blocks and strong earthquakes in the continent of China, *Science in China Series D: Earth Sciences* **46**, 13-24.

Zhang, Z. W., F. Long, X. Y. Zhao, and D. Wang (2022). Study on focal mechanism solution and stress field characteristics in Sichuan and Yunnan area (in Chinese), *Seismology and geology* **44**, no. 1, 170-187.

Zhao, J., J. W. Ren, J. Liu, C. S. Jiang, X. X. Liu, H. B. Liang *et al.* (2020). Coupling fraction and relocking process of the Longmenshan fault zone following the 2008 MW7.9 Wenchuan earthquake, *Journal of Geodynamics* **137**, 101730.

Zhao, M., Z. W. Xiao, S. Chen, and L. H. Fang (2022). DiTing: A large-scale Chinese seismic benchmark dataset for artificial intelligence in seismology, *Earthquake Science* **35**, 1-11.

Zhao, M., Z. W. Xiao, M. Zhang, Y. Yang, L. Tang, and S. Chen (2023a). DiTingMotion: A deep-learning first-motion-polarity classifier and its application to focal mechanism inversion, *Frontiers in Earth Science* **11**, 1103914.

Zhao, Y., J. L. Li, J. Xu, H. J. Yao, G. H. Zhu, H. F. Yang, J. Y. Zahng, and R. Q. Lu 2023. High-resolution velocity structure and seismogenic potential of strong earthquakes in the Bamei-Kangding segment of the Xianshuihe fault zone, *Science China Earth Sciences* **66**, no. 9, 1960-1978.

Zheng, Y., R. M. Guo, and D. C. Liu, (2024). Present status and prospective on the seismic hazard studies of major seismic gaps in the Sichuan-Yunnan region, *Science China Earth Sciences* **67**, no. 11, 3339-3366.

Zhou, R. J., Y. L. He, Z. Z. Huang, X. G. Li, and T. Yang (2001a). The slip rate and strong earthquake recurrence interval on the Qianning-Kangding segment of the Xianshuihe fault zone, *Acta Seismology Sinica* **23**, no. 3, 250-261.

Zhou, Y. J., H. Yue, L. H. Fang, S. Y. Zhou, L. Zhao, and A. Ghosh (2021). An earthquake detection and location architecture for continuous seismograms: phase picking, association, location, and matched filter (PALM), *Seismological Research Letters* **93**, 413-425.

Zhou, Y. J., H. Yue, S. Y. Zhou, L. H. Fang, Y. Zhou, L. S. Xu, *et al.* (2022). Microseismicity along Xiaojiang fault zone (southeastern tibetan plateau) and the characterization of interseismic fault behavior, *Tectonophysics* **833**, 229364.

Zhou, Y. J., H. Y. Ding , A. Ghosh, and Z. X. Ge (2025). AI-PAL: Self-supervised AI phase picking via rule-based algorithm for generalized earthquake detection, *Journal of Geophysical Research: Solid Earth* **130**, e2025JB031294.

Zhu, W. Q., J. H. Song, H. Y. Wang, and J. Munchneyer (2025). Towards End-to-End Earthquake Monitoring Using a Multitask Deep Learning Model, arXiv preprint arXiv:2506.06939.

Zhu, Y. G., F. Q. Diao, F. Chen, Y. B. Wang, Z. G. Shao, R. J. Wang, and X. Xiong (2024). Probing the interseismic locking state of the Xianshuihe fault based on a viscoelastic deformation model, *Science China Earth Sciences* **67**, no. 1, 134-145.

Zi, J. P., Y. Y. Yang, H. F. Yang, and J. R. Su (2025). The 11-month precursory fault activation of the 2019 ML 5.6 earthquake in the Weiyuan shale gas field, China, *Communications Earth and Environment* **6**, 175.

Full mailing address for each author

Ziyi Li: Institute of Geophysics, China Earthquake Administration
No.5, Minzudaxue South Road, Haidian District, Beijing 100081, China
School of Earth and Space Sciences, Peking University
No.5, Yiheyuan Road, Haidian District, Beijing 100871, China
Lianqing Zhou: Key Laboratory of Earthquake Prediction, Institute of Earthquake Forecasting, China Earthquake Administration
No.63, Fuxing Road, Haidian District, Beijing 100036, China
Mengqiao Duan: Key Laboratory of Earthquake Prediction, Institute of Earthquake Forecasting, China Earthquake Administration
No.63, Fuxing Road, Haidian District, Beijing 100036, China
Yanru An: China Earthquake Networks Center
No.5, Sanlihe South Road, Xicheng District, Beijing 100045, China
Zheng Wu: China Earthquake Networks Center
No.5, Sanlihe South Road, Xicheng District, Beijing 100045, China
Lisheng Xu: Institute of Geophysics, China Earthquake Administration
No.5, Minzudaxue South Road, Haidian District, Beijing 100081, China
Shiyong Zhou: School of Earth and Space Sciences, Peking University
No.5, Yiheyuan Road, Haidian District, Beijing 100871, China

List of Figure Captions

Figure 1. Tectonic setting and stations of the Sichuan-Yunnan region.

Figure 2. Comparison of picking accuracy of the three AI pickers.

Figure 3. 3 × 3 confusion matrices for P-wave first-motion polarity picking results.

Figure 4. Map view of 10-year (2013-2022) relocation catalog in the Sichuan-Yunnan region.

Figure 5. Map view and depth profiles of the earthquakes along the LMS (C1).

Figure 6. Map view and depth profiles of the earthquakes along the XSH (C2).

Figure 7. Map view of the earthquakes in the C3, C4 and C5.

Figure 8. Map view of 10-year focal mechanism catalog, and 0.25° × 0.25° resolved stress field mode in the Sichuan-Yunnan region.

Figure 9. Stress field model for the LMS in different depth ranges.

Figure 10. Maps of b-value in the XSH at different periods.

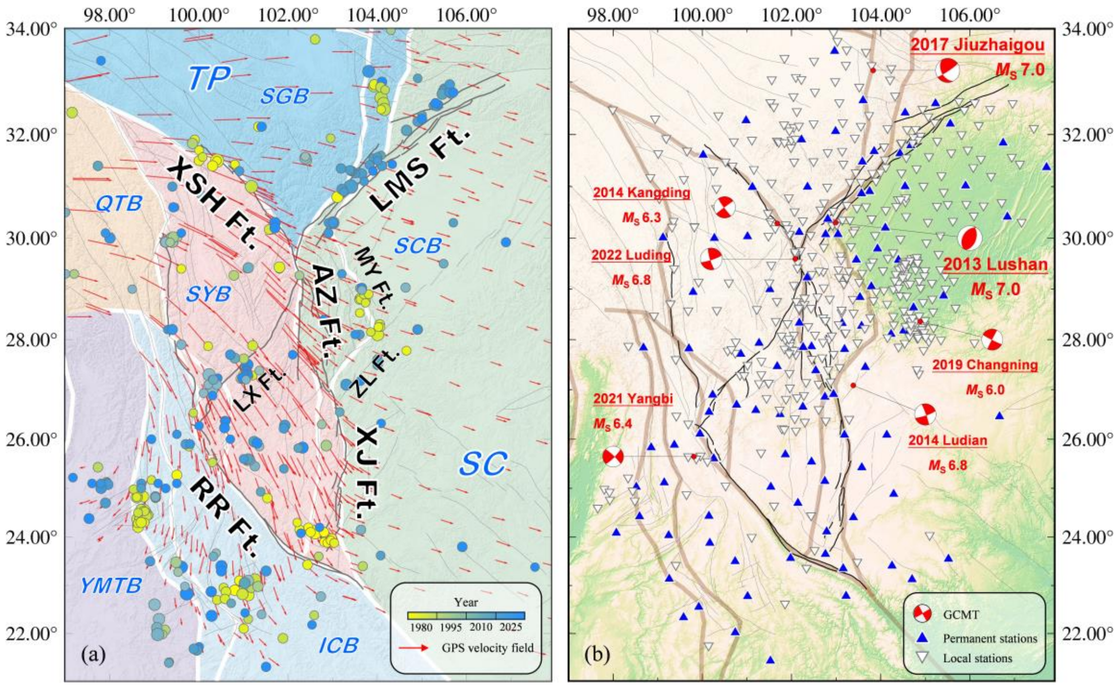

Figure 1. (a) Tectonic setting, historical earthquakes and GPS velocity field of the Sichuan-Yunnan region. Historical earthquakes (1970-) of magnitudes M > 5 are denoted by the colored circles. GPS velocity field (Wang and Shen, 2020) are denoted by the red arrow. Black lines depict active faults. Solid white lines represent block boundaries. (b) Permanent stations (blue triangles, 101) and local stations (white triangles, 413) used in this study. The red focal spheres are earthquakes of magnitudes $M_S > 6$ in the study period (2013-2022) from the GCMT catalog.

The Sichuan-Yunnan region is divided into colored secondary blocks by black major fault zones. Historical earthquakes since 1970 cluster along block boundaries, while red focal spheres mark major earthquakes from 2013 to 2022. Blue triangles indicate permanent stations and white triangles indicate local stations distributed around the fault zones.

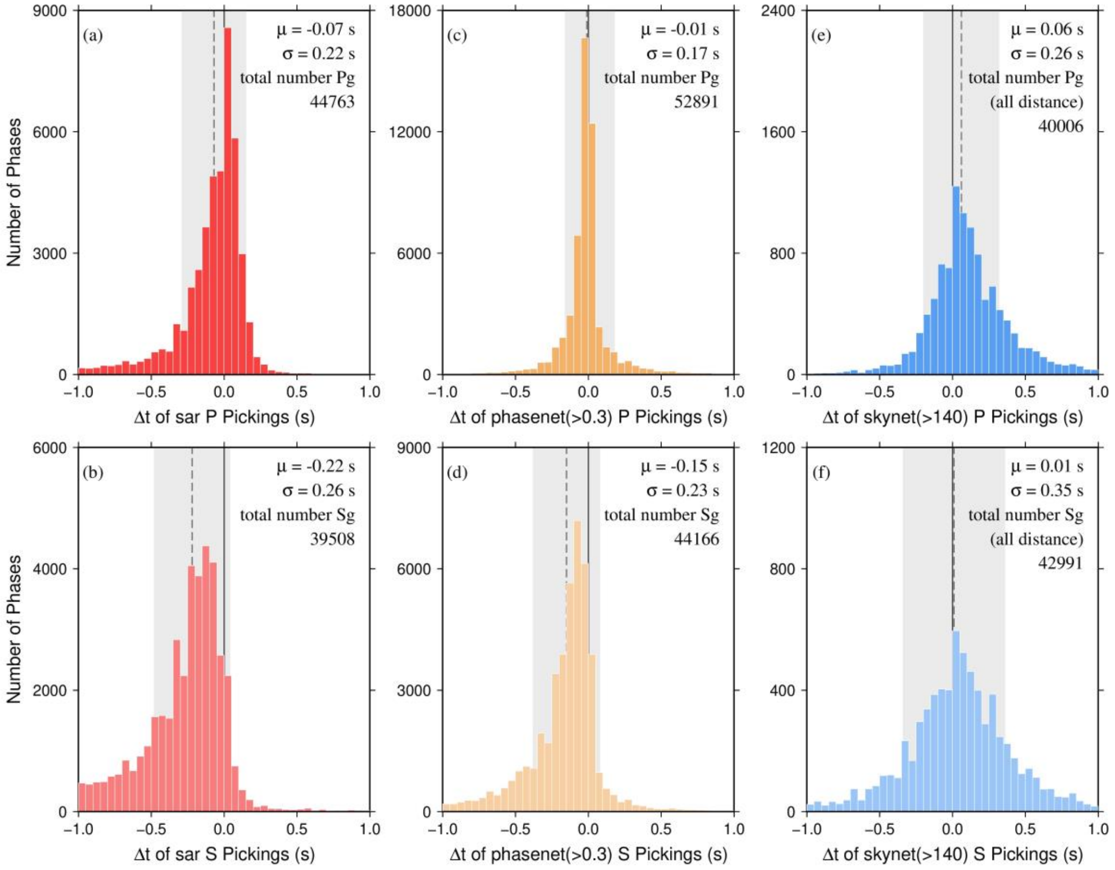

Figure 2. Comparison of picking accuracy of the three AI pickers: SAR (a, b), PhaseNet+ (c, d) and SKYNET (e, f). Δt represents picking errors, defined as manually-picked arrivals minus AI-based arrivals. The black line represents the reference position with Δt is 0, the gray dotted line represents the mean Δt of phase-pickers, and the gray area marks the range of standard deviation.

Six panels comparing picking accuracy for SAR, PhaseNet+, and SKYNET. The more the histogram clusters toward the center, the smaller the picking error.

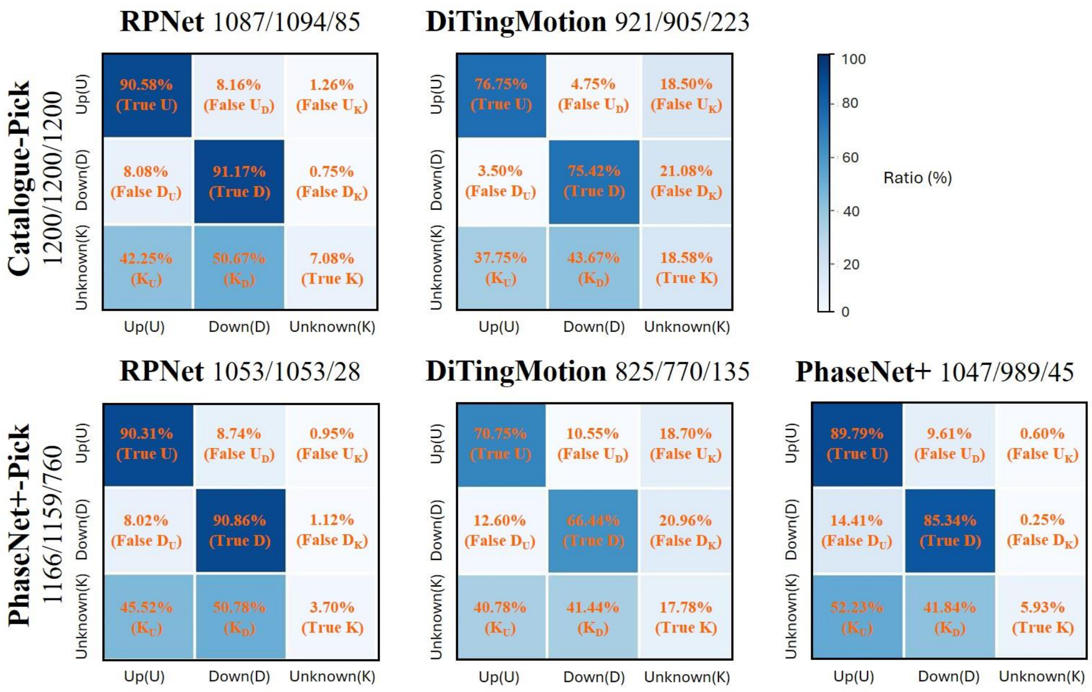

Figure 3. 3 × 3 confusion matrices for P-wave first-motion polarity picking results (up, down, and unknown). The tow row shows picking results for RPNet and DiTingMotion using accurate P-wave arrival times, with 1,200 samples each for the up, down, and unknown labels from the manual catalog. The bottom row displays results for RPNet, DiTingMotion, and PhaseNet+ based on arrival times picked by PhaseNet+, which identified 1,166, 1,159, and 760 polarities corresponding to the manual labels, respectively. Subpanel titles indicate the quantity of polarities picked by each method, and orange numbers represent the percentages of correct or incorrect picks. Definitions are as follows: TrueU, TrueD, and TrueK denote correctly identified up, down, and unknown polarities; $\mathrm{FalseU_D}$ and $\mathrm{FalseU_K}$ represent up polarities misidentified as down or unknown; $\mathrm{FalseD_U}$ and $\mathrm{FalseD_K}$ represent down polarities misidentified as up or unknown; $\mathrm{K_U}$ and $\mathrm{K_D}$ denote unknown polarities misidentified as up or down.

Five 3 × 3 confusion matrices comparing P-wave polarity picking for RPNet, DiTingMotion, and PhaseNet+ using the accurate arrival times and PhaseNet+ picked arrivals. The orange numbers in the cell indicate the pick-up effect.

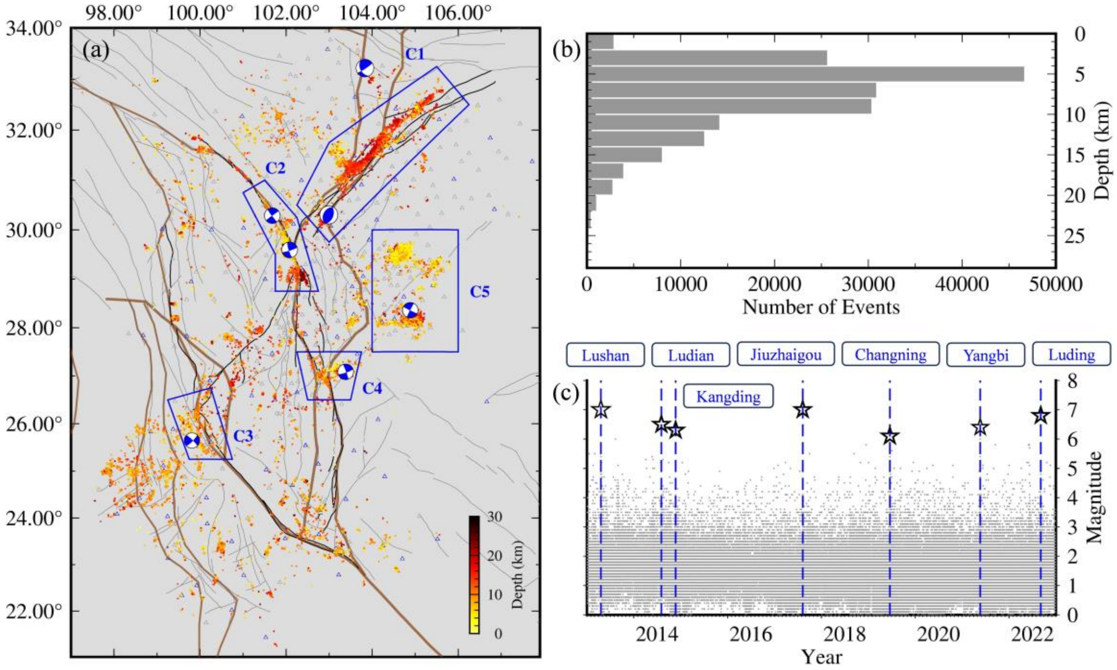

Figure 4. (a) Map view of 10-year (2013-2022) relocation catalog of the Sichuan-Yunnan region. The blue focal spheres are same as figure1b. Blue polygons show subregions. (b) Seismic depth histogram. (c) Magnitude versus time series statistics. The black star represents 7 earthquakes with $M_S > 6.0$ marked by the blue focal spheres in (a).

The spatial distribution of relocated catalogs, distribution with depth, and distribution over time. Spatially, they are concentrated around the main fault zones, and in depth, they are mainly between 5-15 km.

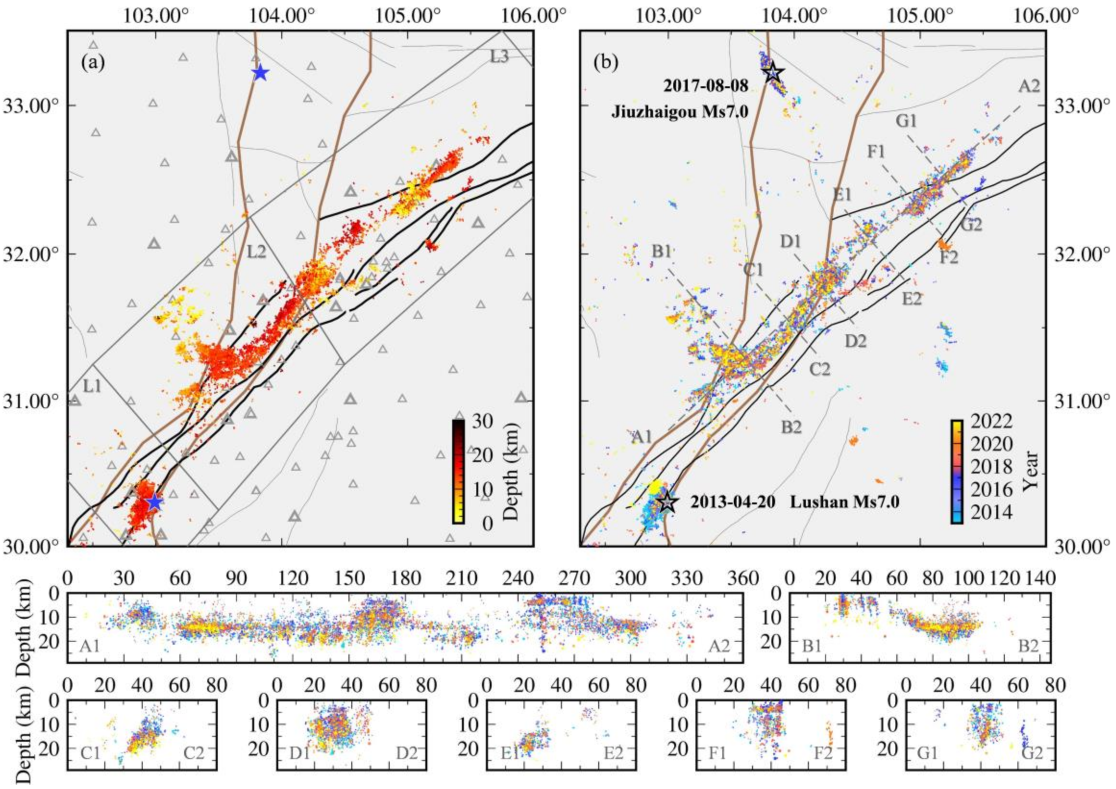

Figure 5. Map view and depth profiles of the earthquakes along the LMS (C1). Circles color coded by depth (a) and time (b). Gray polygons represent the segmentation of the fault zone. The positions of profiles A1-A2 to G1-G2 are shown in (b) with gray dashed. Seismicity of the Longmenshan fault zone with depth and time distribution, as well as some depth profiles along the strike and the vertical direction of the fault.

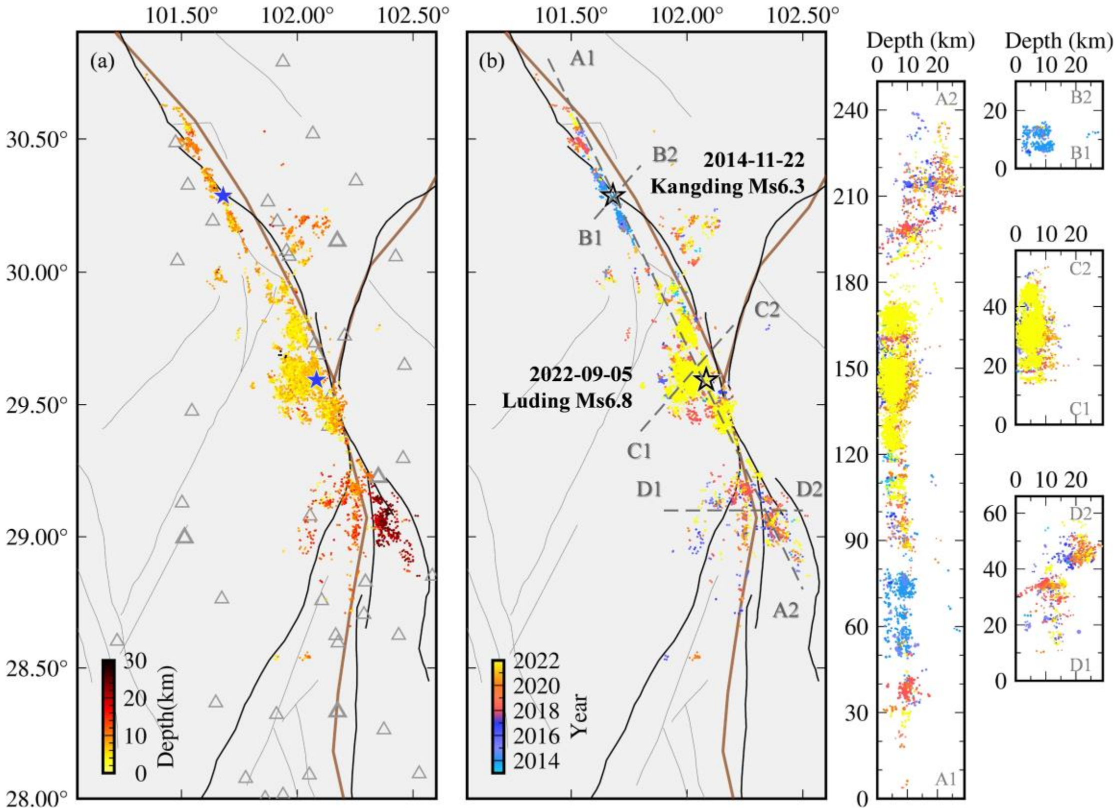

Figure 6. Map view and depth profiles of the earthquakes along the XSH (C2). Circles color coded by depth (a) and time (b). The positions of profiles A1-A2 to D1-D2 are shown in (b) with gray dashed.

Seismicity of the Xianshuihe fault zone with depth and time distribution, as well as some depth profiles along the strike and the vertical direction of the fault.

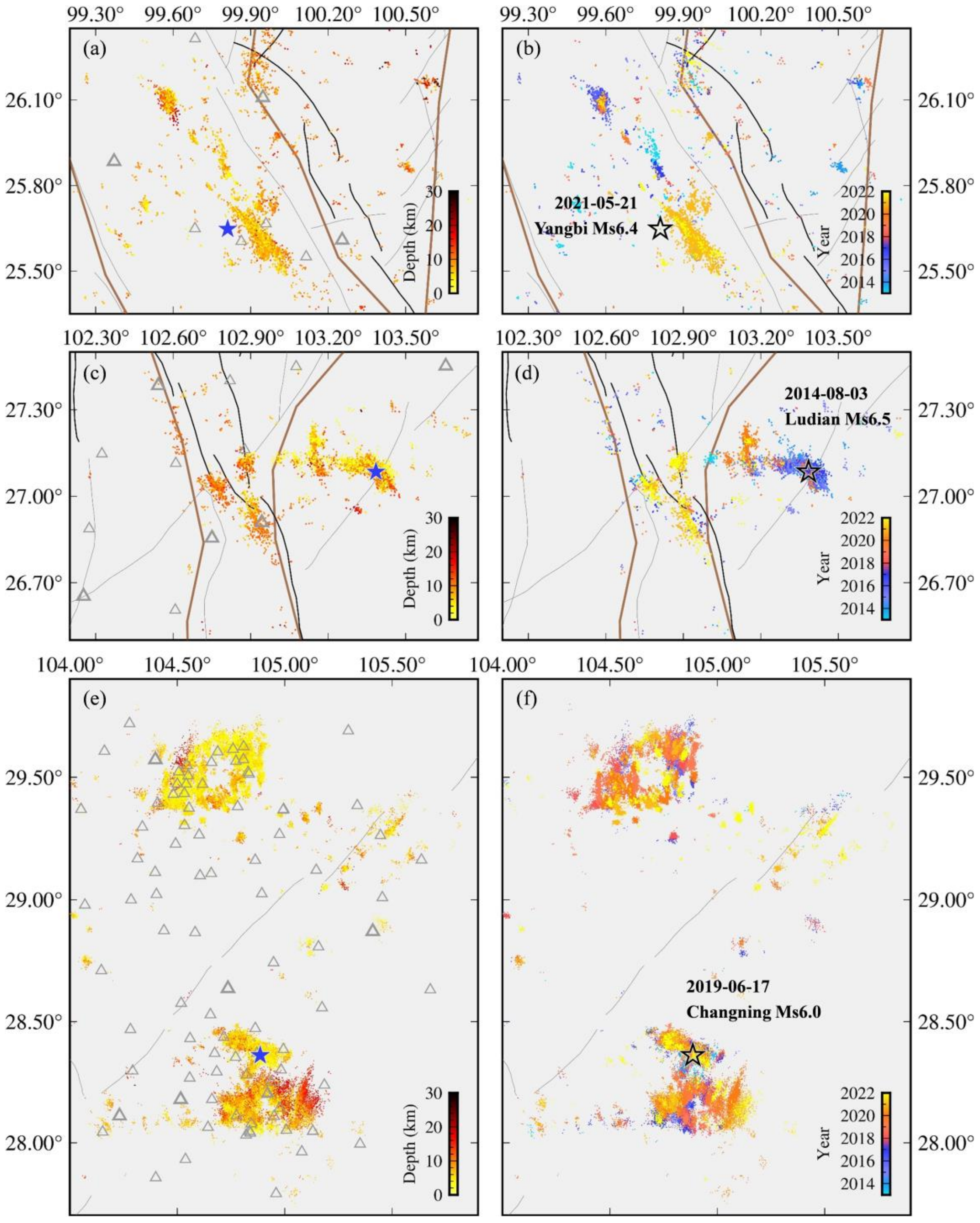

Figure 7. Map view of the earthquakes in the C3 (a, b), C4 (c, d) and C5 (e, f). Circles color coded by depth (a, c, e) and time (b, d, f).

Seismicity of the Red River fault, the northern section of Xiaojiang fault, and southern Sichuan Basin with depth and time distribution.

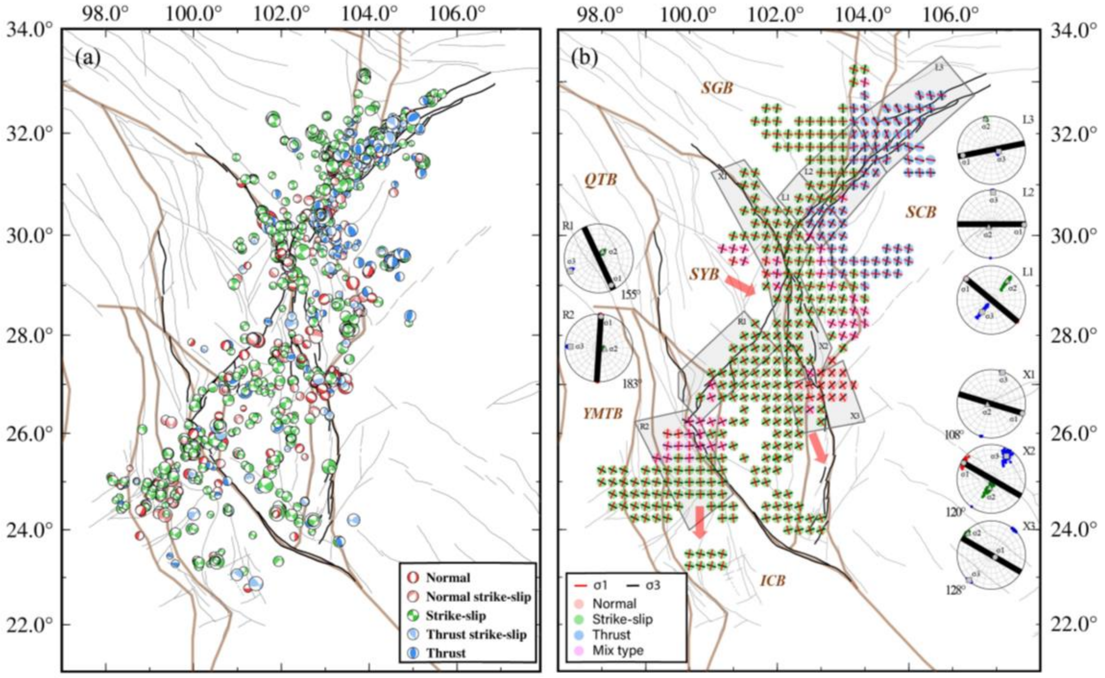

Figure 8. (a) Map view of 10-year focal mechanism catalog of the Sichuan-Yunnan region. Focal spheres color indicates the different types. (b) Map view of 0.25° × 0.25° resolved stress field model, and average principal stress axes of the major active faults: LMS (L1, L2 and L3), XSH (X1), AZ (X2), northern segment of XJ (X3), LX (R1), and RR (R2).

Focal spheres of different types indicated by different colors are distributed along major faults in the Sichuan-Yunnan region. 0.25° × 0.25° resolved stress field model includes the stress type represented by colors and the principal stress direction information, with the average stress direction of the main fault zones drawn in the circle beside it.

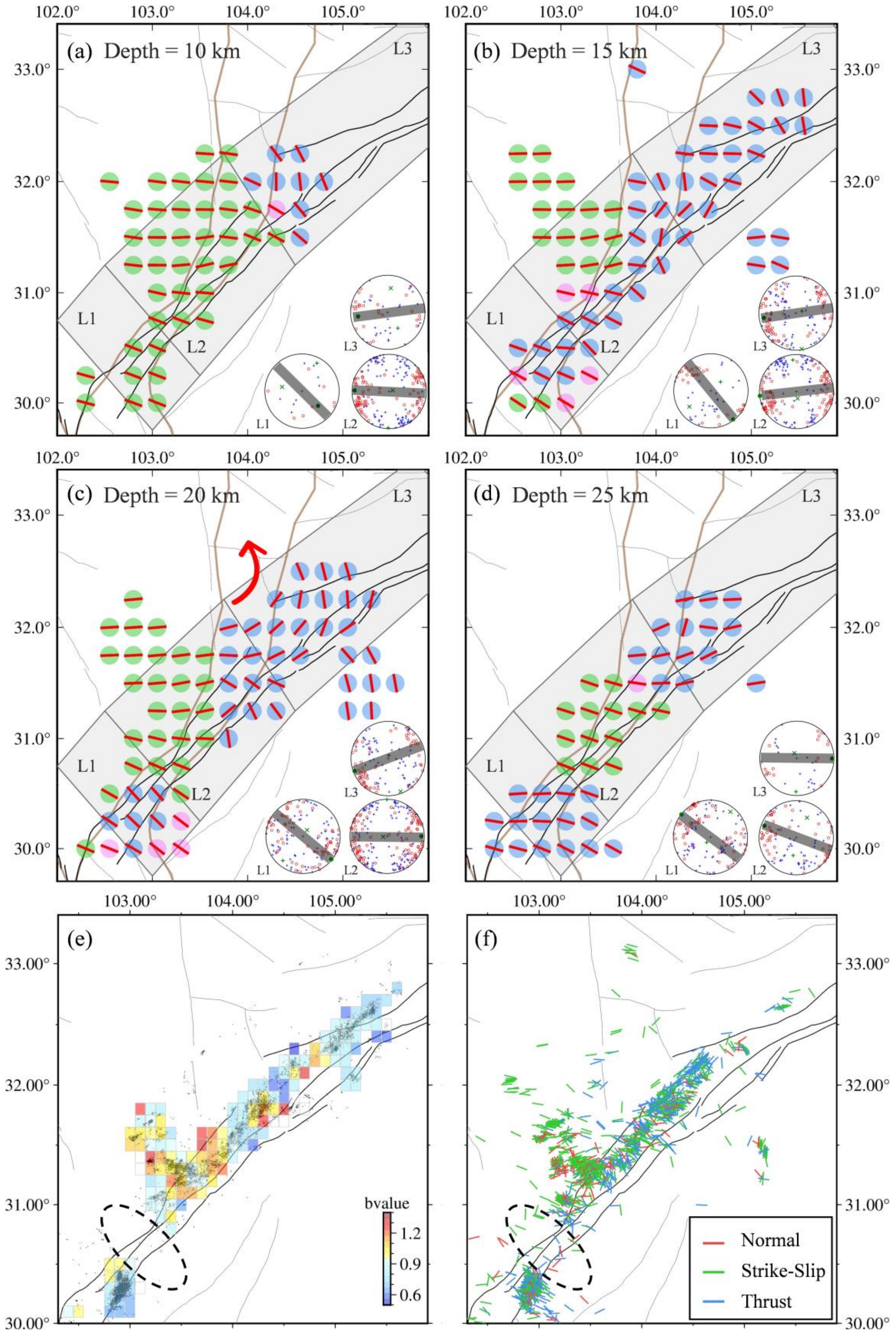

Figure 9 (a-d) Map view of 0.25° × 0.25° resolved stress field model for the LMS in different depth ranges, and average principal stress axes of the segments L1, L2 and L3.

Map of b-value (e) and P-axis azimuth (f) along the LMS. The black dotted circle indicates the Dayi seismic gap.

Stress type represented by colors and the principal stress direction information at different depths of the Longmenshan fault zone. The other two panels showing the spatial variation of the b-value in the Longmenshan fault zone, and the P-axis angle of each earthquake.

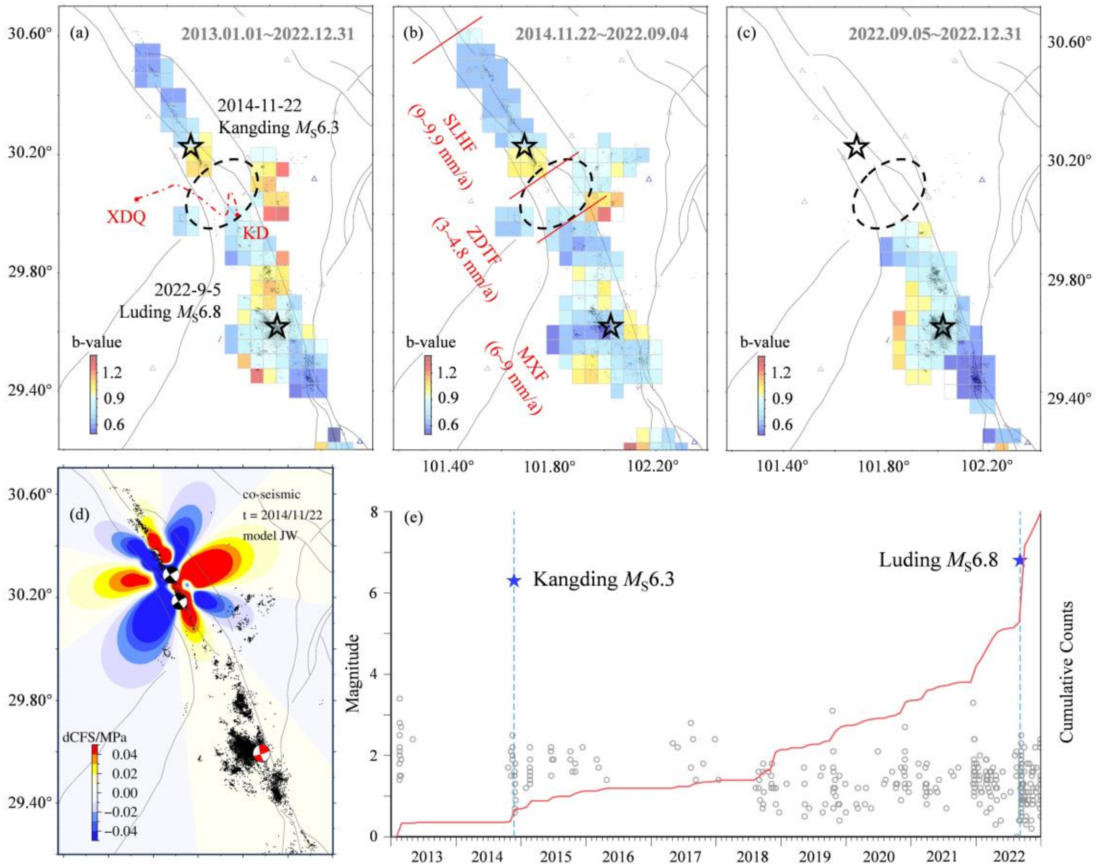

Figure 10 (a-c) Maps of b-value in the XSH at different periods. The red dotted line represents the approximate location of the Sichuan-Tibet Railway from Xinduqiao to Kangding (Li et al., 2022). The black dotted circle indicates the Zheduotang fault seismic gap. (d) Spatial distribution of the coseismic Coulomb failure stress change on the XSH induced by the Kangding M_S 6.3 earthquake. (e) Magnitude versus time series statistics in the Zheduotang fault seismic gap (black dotted circle in a). The red curve

indicates the cumulative number of earthquakes.

The first three panels showing the spatial variation of the b-value in the Xianshuihe fault zone over different time periods. The other two panels showing the distribution of earthquakes along the Xianshuihe fault over time, and the coseismic stress impact of the Kangding earthquake on the surrounding area.

Supplementary Information for

Seismological models based on a hybrid deep-learning strategy reveal tectonic features and earthquake risk in the Sichuan-Yunnan region

Ziyi Li[1,2], Lianqing Zhou[3*], Mengqiao Duan[3], Yanru An[4], Zheng Wu[4],
Lisheng Xu[1] & Shiyong Zhou[2]

1. Institute of Geophysics, China Earthquake Administration, Beijing 100081, China
2. School of Earth and Space Sciences, Peking University, Beijing 100871, China
3. Key Laboratory of Earthquake Prediction, Institute of Earthquake Forecasting, China Earthquake Administration, Beijing 100036, China
4. China Earthquake Networks Center, Beijing 100045, China

Corresponding author: Lianqing Zhou (zhoulq@ief.ac.cn)

List of Supplemental Table Captions

Table S1. Quality grades of focal mechanism defined by SKHASH

Table S2. Focal mechanisms types based on the areal strain.

List of Supplemental Figure Captions

Figure S1. Distance reported by manually-picked phases of permanent network in 2013.

Figure S2. Variation of Δt with distance

Figure S3. Distances distribution of missing phases.

Figure S4. Relationship between misclassified polarities and magnitude or distance.

Figure S5. Relationship between misclassified polarities and stations.

Figure S6. Comparison between manual catalog and PAL associated catalog.

Figure S7. Picking accuracy and probability distribution of Pg and Sg wave.

Figure S8. Travel time versus hypocentral distance of associated events.

Figure S9. Phase picking and association, two examples of small earthquakes.

Figure S10. Map view of earthquakes in five subregions based on the manual catalog.

Figure S11. The polarity misfit, the plane uncertainty, the station distribution ratio, and the probability of the best-fitting mechanism of focal mechanism with different quality grades.

Figure S12. The polarity misfit, the plane uncertainty, the station distribution ratio, and the probability of the best-fitting mechanism of focal mechanism with class A and B

Figure S13. Magnitude of focal mechanism with class A and B.

Table S1. Quality grades of focal mechanism defined by SKHASH. "Average misfit" (0-1) measures the mismatch between the observed polarity and the theoretical polarity of the model inversion. "RMS plane uncertainty" measures the uncertainty of fault plane. A small value indicates that solution is stable. "Station distribution ratio" (0-1) measures the distribution of stations projected onto the source sphere. A small value indicates that the stations are concentrated near the nodal plane. "Mechanism probability" (0-1) measures the probability of the best mechanism solution.

Quality grade	Average misfit	RMS plane uncertainty	Station distribution ratio	Mechanism probablity
A	≤0.15	≤25°	≥0.5	≥0.8
B	≤0.20	≤35°	≥0.4	≥0.6
C	≤0.30	≤45°	≥0.3	≥0.5
D	>0.30	>45°	>0.3	>0

Table S2. Focal mechanisms types based on the areal strain (A_S). A_S is the sum of the principal compressive strain and the tensile strain. When $A_S>0$, it indicates an overall dilatation, corresponding to the thrust component; When $A_S<0$, it indicates overall compression, corresponding to normal component; $A_S=0$ indicates strike slip fault.

Normal fault type (NF)	$-1 \le A_S \le -0.7$
Normal fault with strike-slip components (NS)	$-0.7 \le A_S \le -0.3$
Strike-slip type (SS)	$-0.3 \le A_S \le 0.3$
Thrust with strike-slip components (TS)	$0.3 \le A_S \le 0.7$
Thrust fault type (TF)	$0.7 \le A_S \le 1$

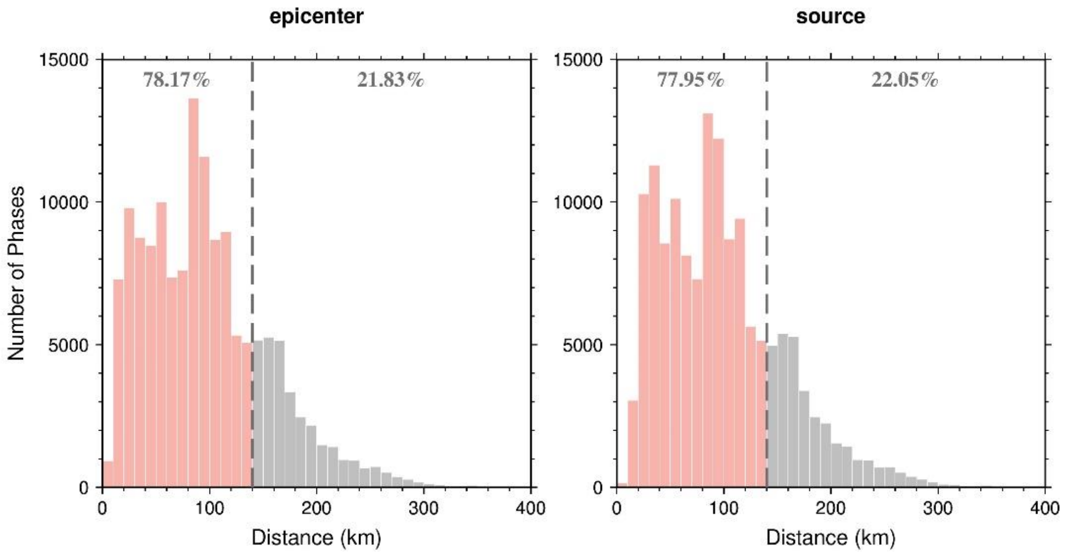

Figure S1. Distance (epicenter distance and source distance) reported by manually-picked phases of permanent network in 2013. The dotted line corresponds to the distance of 140 km.

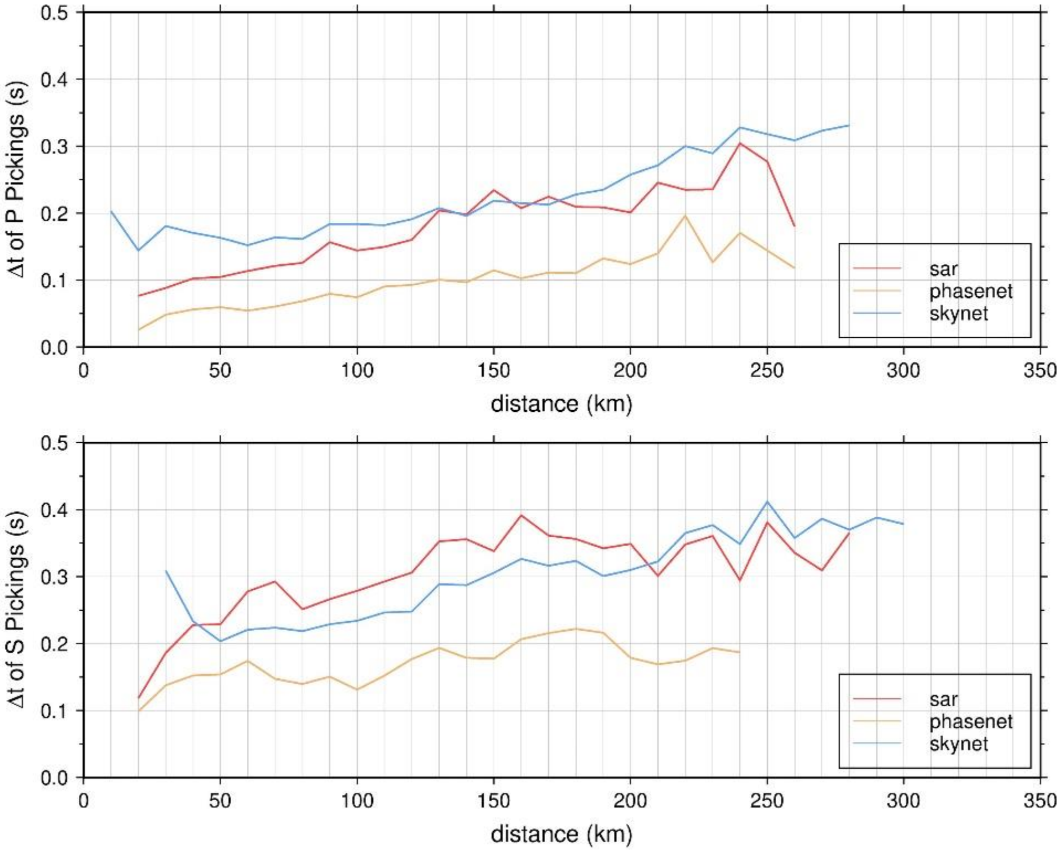

Figure S2. Variation of Δt with distance. The sliding step of the distance is 10 km.

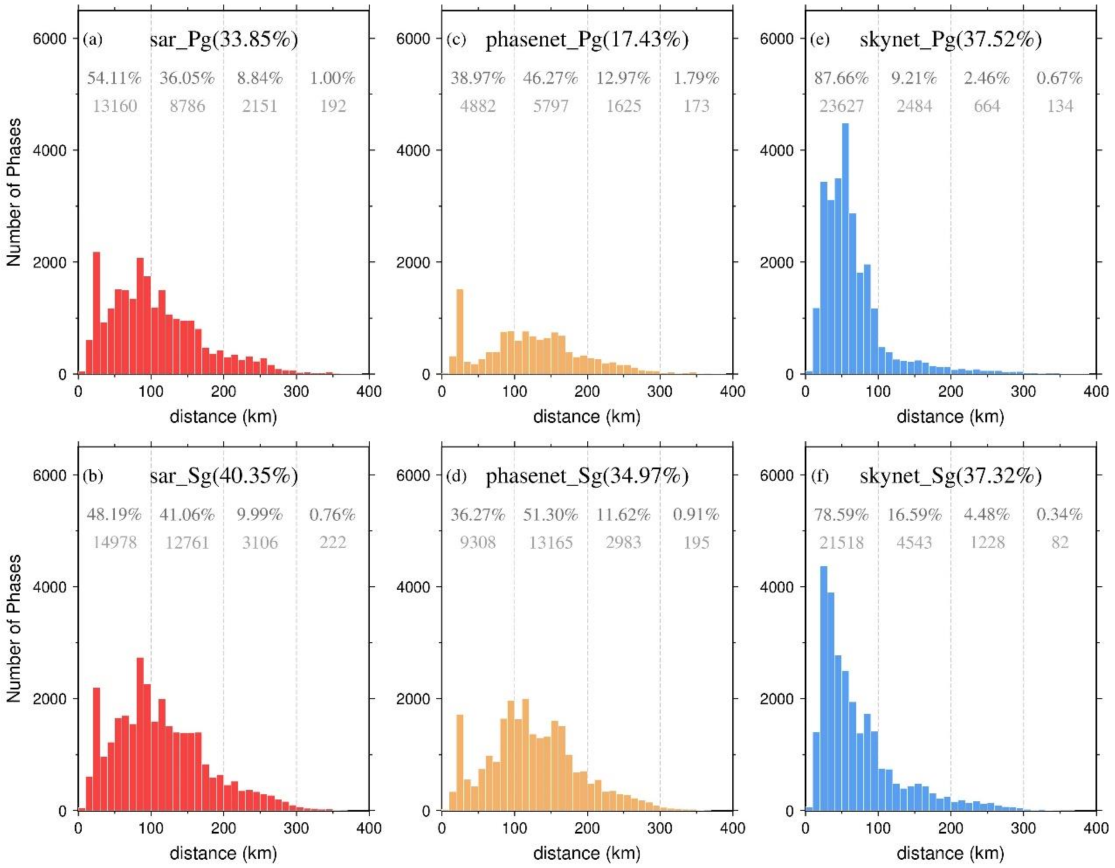

Figure S3. Distances distribution of missing phases. Dotted lines are separated every 100 km.

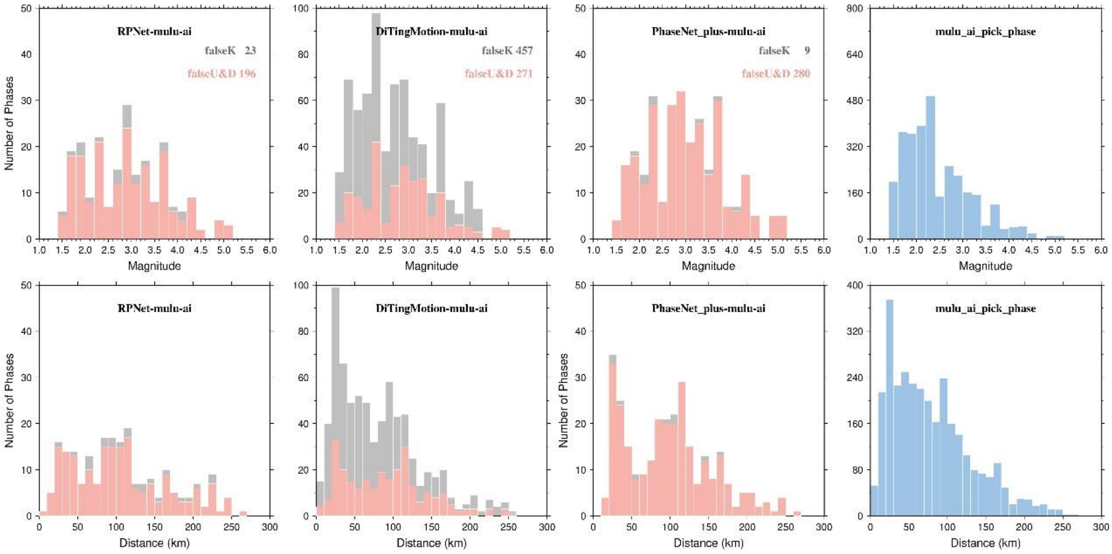

Figure S4. Relationship between misclassified polarities and magnitude (top row) or distance (bottom row). Pink indicates the False UD and False DU. Grey indicates the False UK and False DK. Blue indicates the magnitude and distance statistics of manual labels.

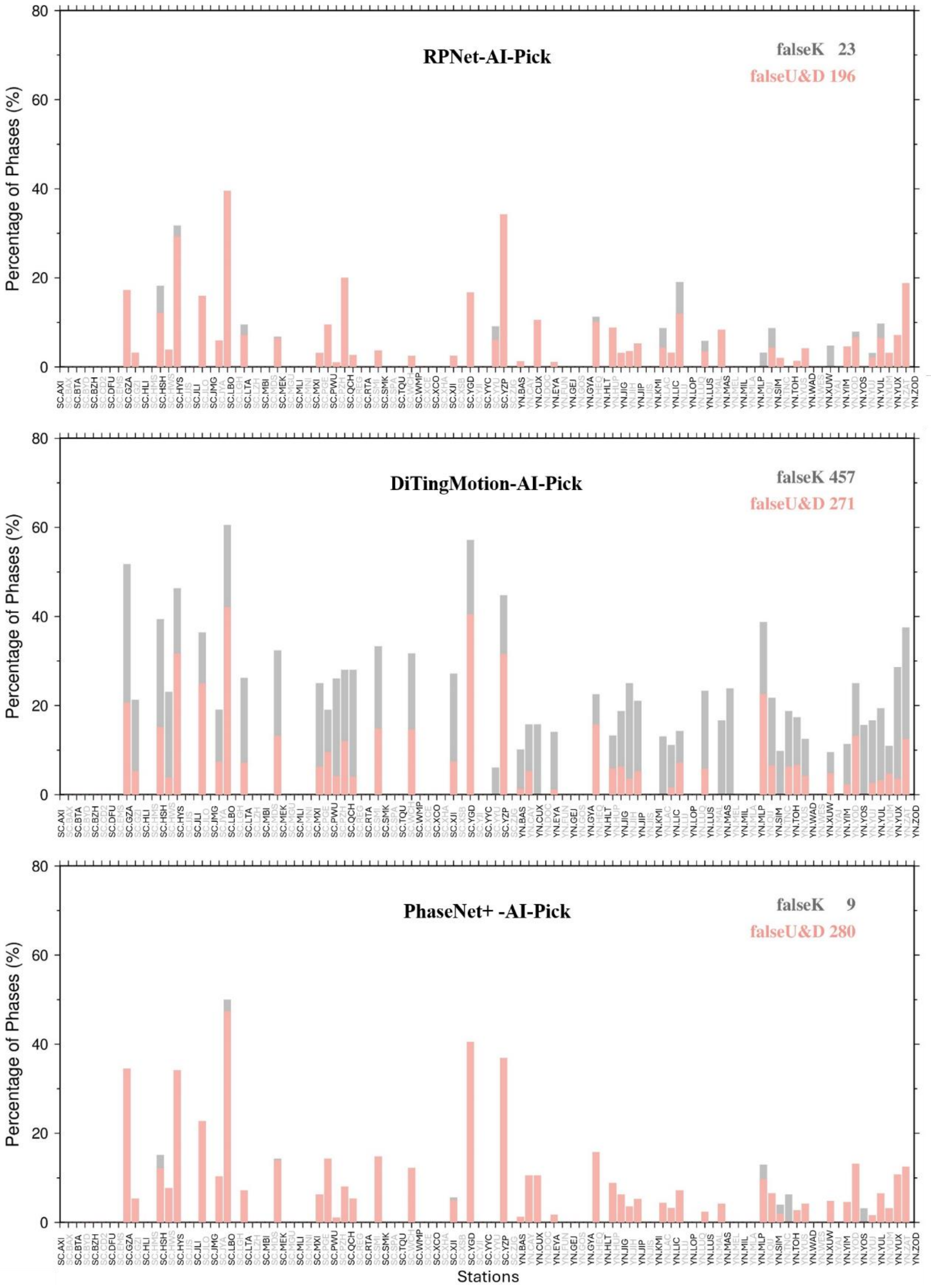

Figure S5. Relationship between misclassified polarities and stations.

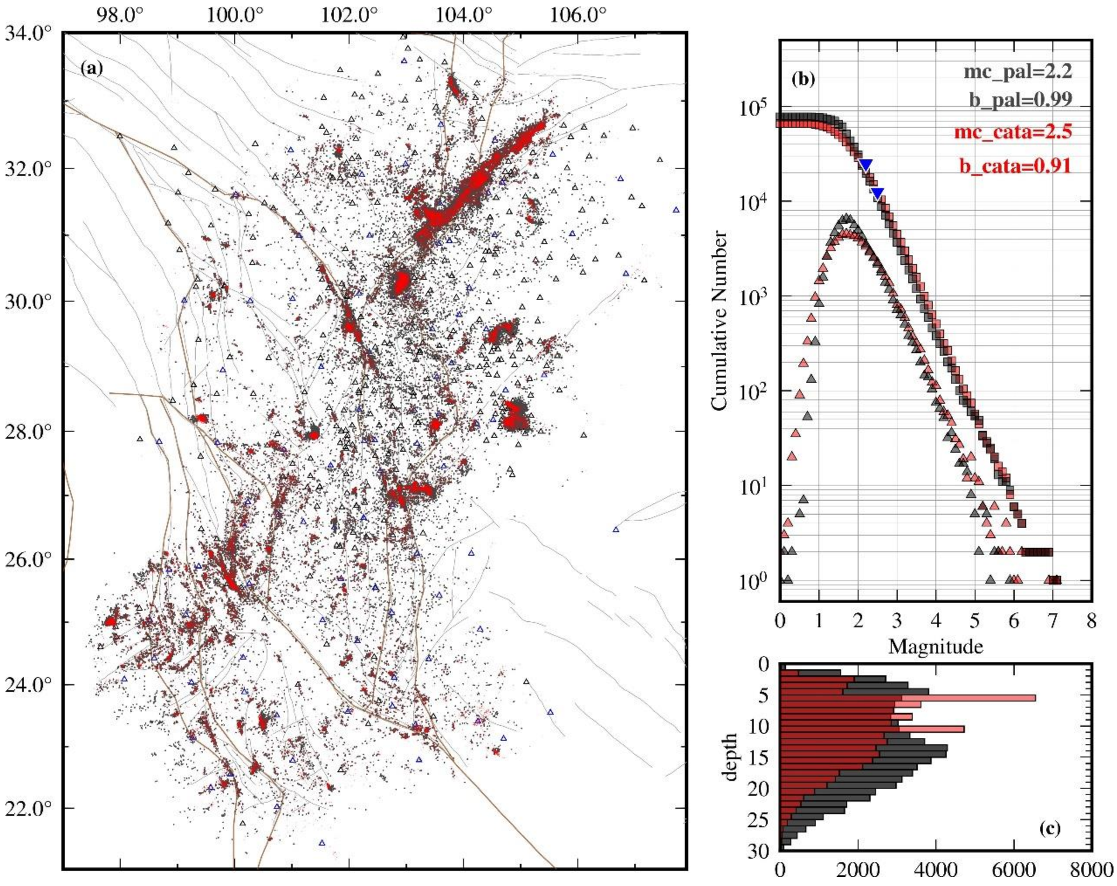

Figure S6. Comparison of map view (a), frequency-magnitude distribution (b), and depth distribution between PAL catalog (grey) and manual catalog (red).

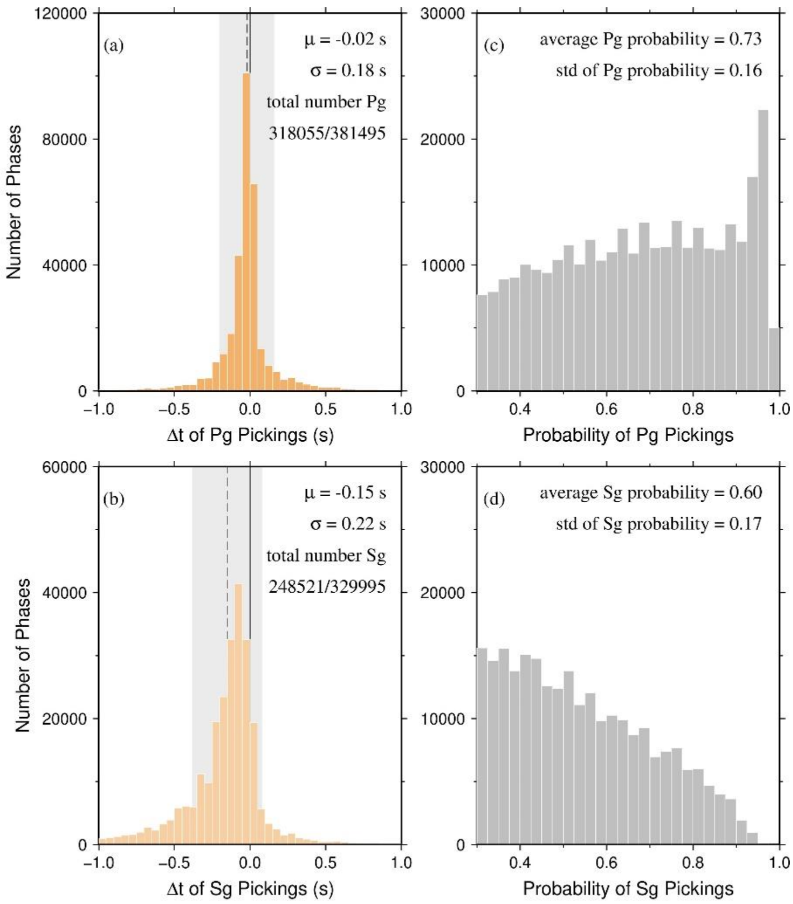

Figure S7. Picking accuracy (a, b) and probability distribution (c, d) of Pg and Sg wave. Δt represents picking errors (manually-picked arrivals - AI-based arrivals). The black line represents the reference position with Δt is 0, the gray dotted line represents the mean Δt of phase-pickers, and the gray area marks the range of standard deviation.

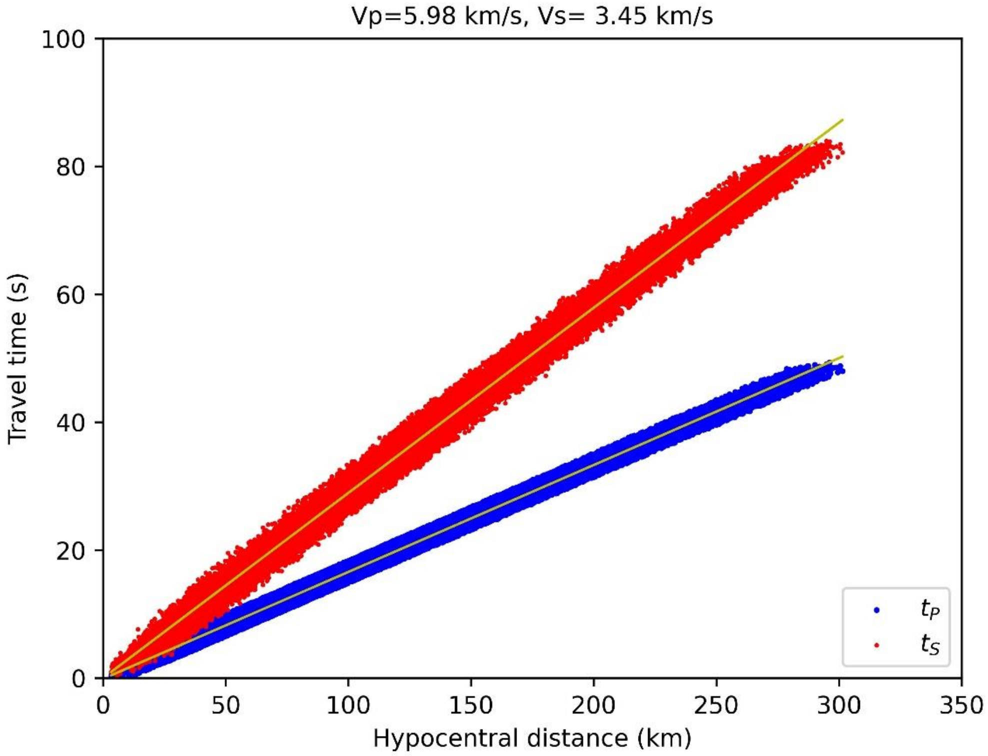

Figure S8. Travel time versus hypocentral distance of associated events.

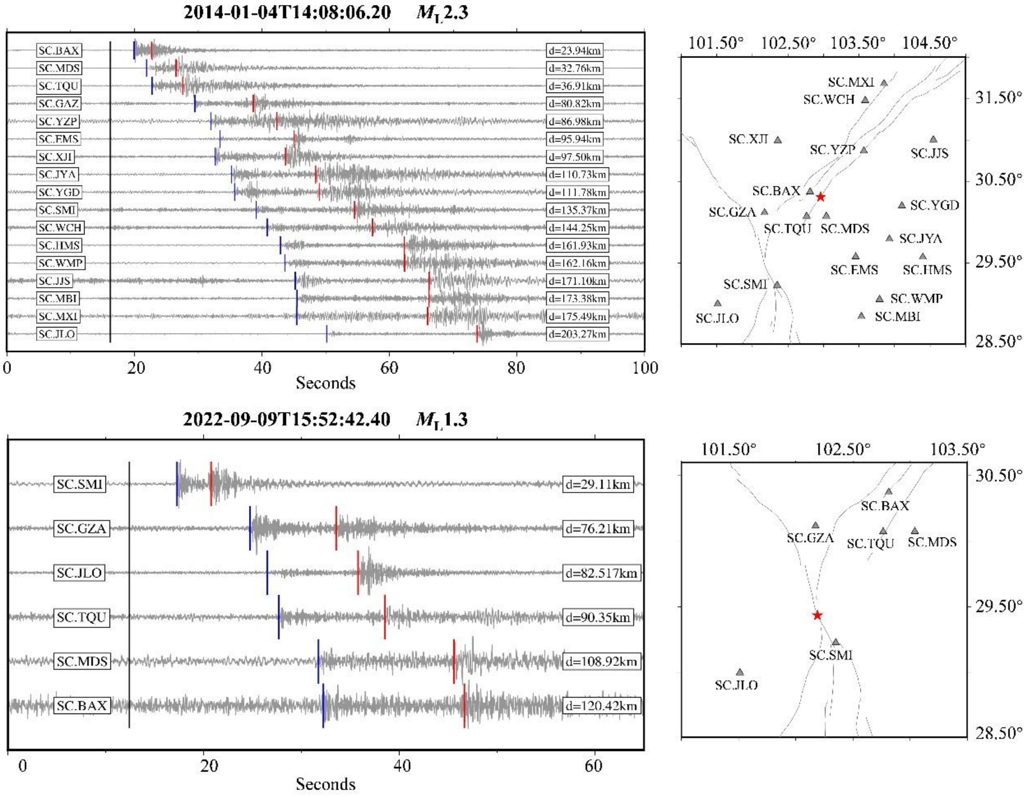

Figure S9. Phase picking and association. Two examples of small earthquakes (M_L2.3 and M_L1.3). Blue and red marks indicate Pg and Sg arrivals, respectively.

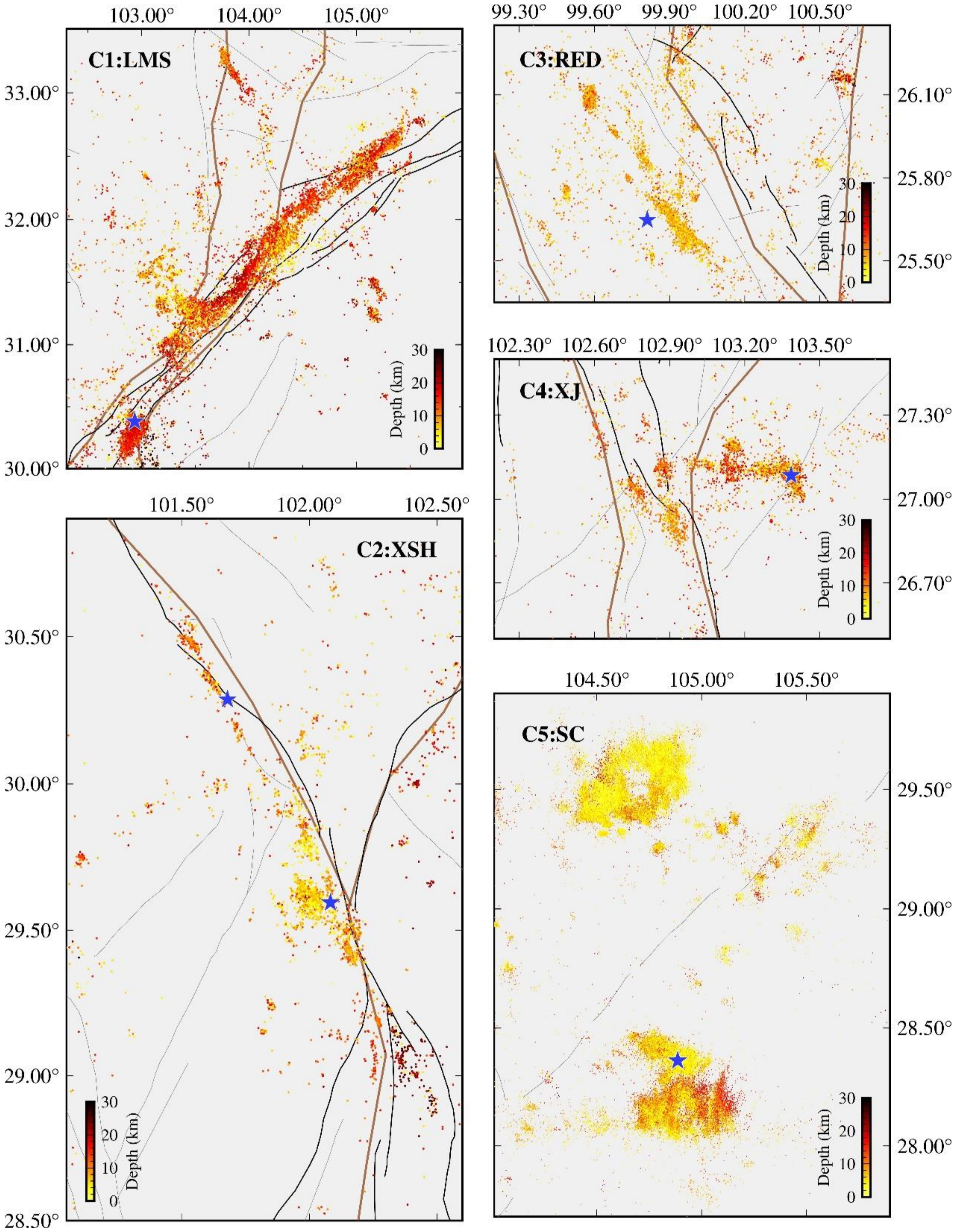

Figure S10. Map view of earthquakes in five subregions based on the manual catalog. Circles color coded by depth.

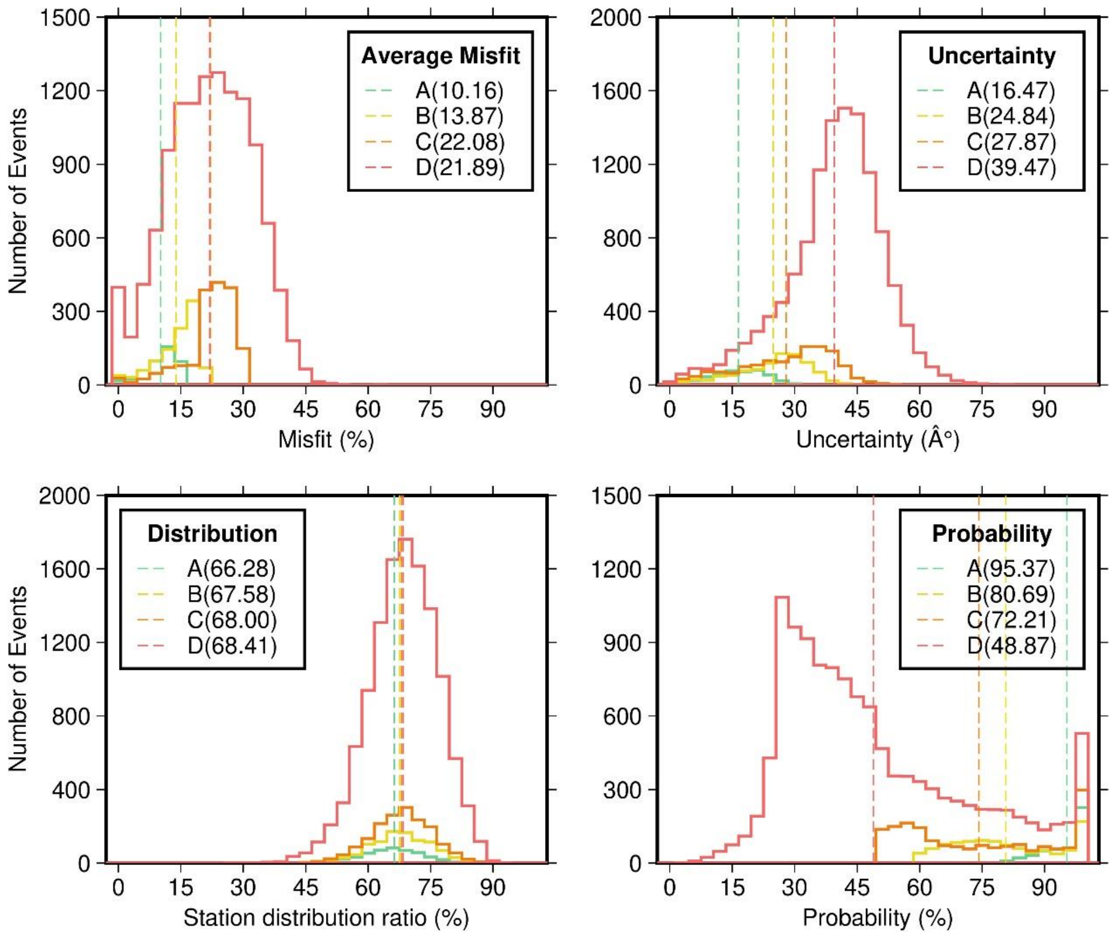

Figure S11. The polarity misfit, the plane uncertainty, the station distribution ratio, and the probability of the best-fitting mechanism of focal mechanism with different quality grades.

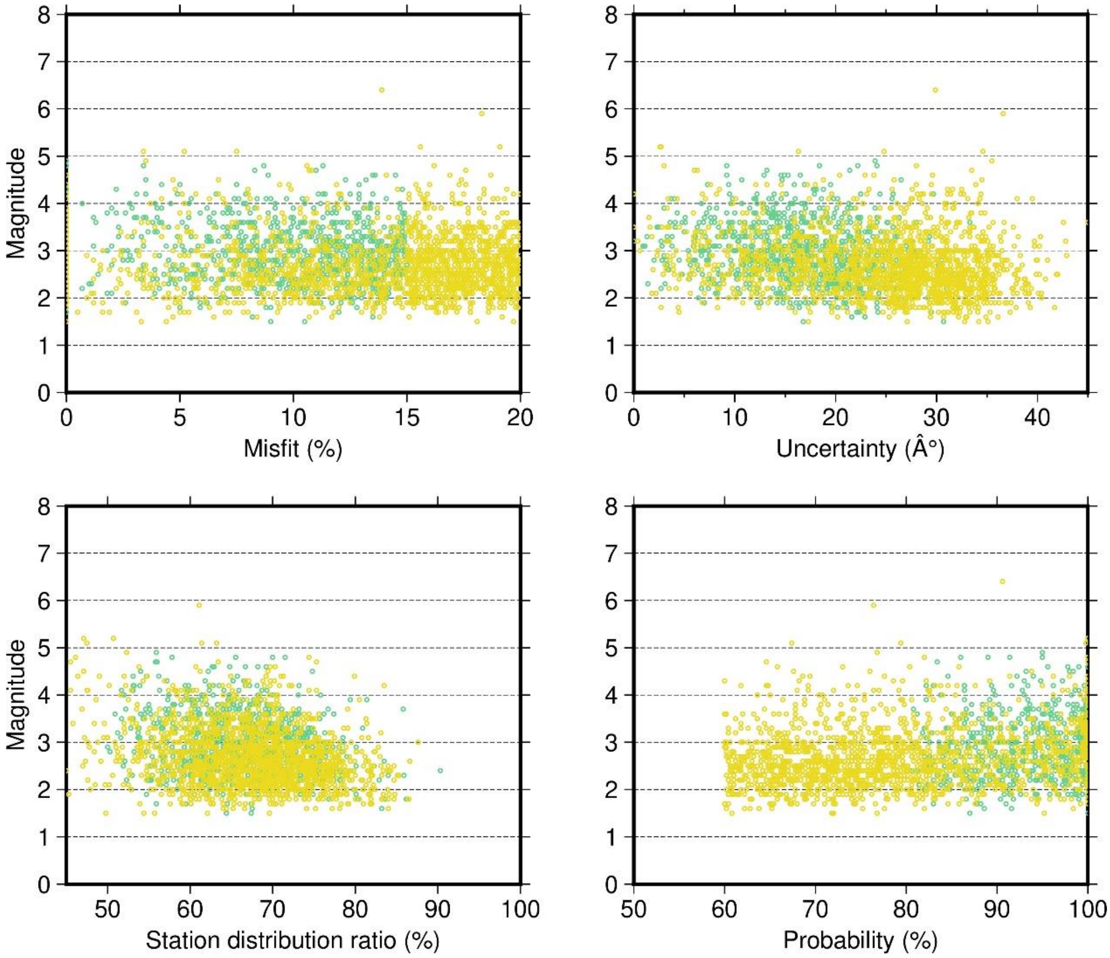

Figure S12. The polarity misfit, the plane uncertainty, the station distribution ratio, and the probability of the best-fitting mechanism of focal mechanism with class A and B.

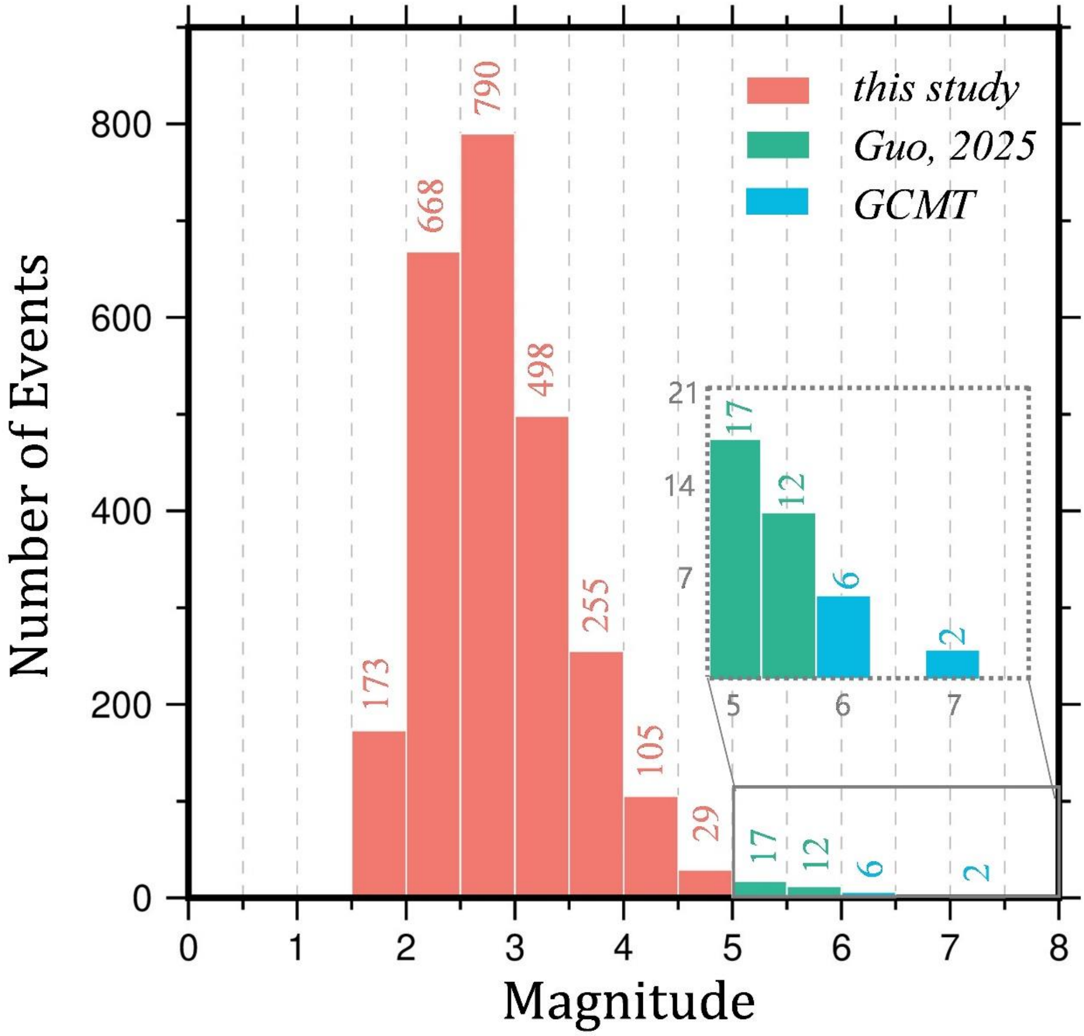

884

885 **Figure S13.** Magnitude of focal mechanism with class A and B.